npj | climate and atmospheric science

Article

Published in partnership with CECCR at King Abdulaziz University

https://doi.org/10.1038/s41612-026-01355-2

Precessional modulation of ENSO strength and spatial structure in a transient CGCM simulation of the past 3 million years

Check for updates

Chao Liu[1], Soon-Il An[2] ✉, Kyung-Sook Yun[3,4], Gagan Mandal[5], Soong-Ki Kim[6], Jong-Seong Kug[1] ✉ & Fei-Fei Jin[7]

A past 3-million-year transient simulation with Community Earth System Model version 1.2 reveals precessional dominance in El Niño–Southern Oscillation (ENSO) variability intensity and spatial structure. Under boreal winter-solstice perihelion (like late Holocene), basin-scale ENSO variability intensifies through strengthened thermocline and zonal advective feedbacks, driven by a broad El Niño-like mean surface warming and enhanced tropical Pacific rainbands. Under boreal vernal-equinox perihelion, central-Pacific ENSO variability shifts eastward moderately, primarily due to intensified zonal advective feedback, following a strengthened background South Pacific Convergence Zone (SPCZ) and interhemispherically opposing rainband changes. ENSO responses under boreal summer-solstice and autumn-equinox perihelion are contrastingly weaker. Consequently, both ENSO characteristics coevolve with the precession's magnitude set by orbital eccentricity. Precessional modulation of ENSO progressively strengthened toward the present, mediated by a gradually intensified background SPCZ under greenhouse gas and ice-sheet forcings. We suggest that sea surface warming patterns and associated tropical rainbands are paramount in past ENSO changes.

El Niño–Southern Oscillation (ENSO) is the leading mode of coupled ocean–atmosphere variability in the tropical Pacific, with profound impacts on the global climate and socioeconomics[1–3]. Climate model projections suggest that ENSO variability may intensify and shift eastward under greenhouse gas warming, although substantial uncertainties remain[4–10]. On longer timescales, variations in Earth's orbital parameters (i.e., eccentricity, obliquity, and precession) also modulate ENSO characteristics and tropical background states by altering top-of-atmosphere (TOA) insolation and perturbing major components of the climate system, such as ice sheets and the Atlantic Meridional Overturning Circulation[11–17]. As such, investigating ENSO behavior under past climate conditions has emerged as a promising avenue for advancing our understanding of ENSO dynamics and its sensitivity to external forcings, and for better constraining projections of future ENSO changes[18–21].

The relatively abundant proxy records enable extensive investigation of ENSO variability during the Holocene (~11.7 thousand years ago, ka, to present) (cf. Lu and Liu, 2018 and references therein)[22]. Both proxy records[23–26] and climate model simulations[27–31] suggest that ENSO variability during the mid-Holocene (~6 ka) was weaker than at present, primarily due to precession-induced changes in seasonal insolation[22,32,33]. Specifically, increased Northern Hemisphere summer insolation around the mid-Holocene strengthened the Asian summer monsoon and induced a La Niña–like mean state cooling in the tropical Pacific by adjusting the zonal Walker circulation, thereby weakening interannual air–sea coupling and ENSO variability[28]. In addition, other mechanisms may also have

[1]School of Earth and Environmental Sciences, Seoul National University, Seoul, Republic of Korea. [2]Department of Atmospheric Sciences, Yonsei University, Seoul, Republic of Korea. [3]Center for Climate Physics, Institute for Basic Science (IBS), Busan, Republic of Korea. [4]Pusan National University, Busan, Republic of Korea. [5]Institute of Earth Atmosphere Astronomy, Yonsei University, Seoul, Republic of Korea. [6]Department of Earth and Planetary Sciences, Yale University, New Haven, CT, USA. [7]Department of Atmospheric Sciences, School of Ocean and Earth Science and Technology (SOEST), University of Hawai'i at Mānoa, Honolulu, HI, USA. ✉e-mail: sian@yonsei.ac.kr; jskug@snu.ac.kr

contributed, including a strengthened cold-tongue seasonal cycle that suppresses ENSO variability through the nonlinear "frequency entrainment" mechanism[32–36], as well as a reduced intensity of extratropical synoptic variability[37] and a strengthened Walker circulation associated with the greening of the Sahara and the resultant enhancement of the West Africa monsoon[38].

In contrast, ENSO changes during the early Holocene remain controversial. While early proxy records[39–41] and most climate model simulations[11,12,18] generally indicate a gradual intensification of ENSO throughout the Holocene, following the monotonic evolution of precessional forcing, some recent high-resolution proxy records[42–44] suggest stronger ENSO activity during the early Holocene than during the mid-Holocene, implying a minimum in ENSO variability during the mid-Holocene. This early Holocene discrepancy partly reflects inherent uncertainties in both data sources, but may also be reconciled by accounting for possible shifts in the ENSO spatial center[45,46] and seasonality[45,47].

For periods earlier than the Holocene, paleo-ENSO studies rely increasingly on numerical model simulations as proxy records become scarce[48]. Snapshot simulations have been widely used to examine ENSO behavior during representative past climate intervals, such as the Last Glacial Maximum (LGM, ~21 ka)[18,29,49,50] and the mid-Pliocene Warm Period (~3 Ma)[51,52]. Nevertheless, owing to the complexity of glacial boundary conditions and forcings, it remains inconclusive whether ENSO variability during the LGM was stronger or weaker than during the preindustrial period (c.f. Lu et al., 2018 and references therein)[48]. The relationship between ENSO variability and the Pacific mean sea surface temperature (SST) zonal gradient also differs across proxy records[40,53] and model simulations[29,54,55]. For the mid-Pliocene, although most models simulate a weaker ENSO relative to the preindustrial climate, changes in the Pacific zonal SST gradient are largely uncertain[52]. Proposed explanations for this weakened ENSO include a northward shift of the Intertropical Convergence Zone (ITCZ) that inhibits ENSO initiation[56] and weakened thermocline feedback associated with a deeper mean thermocline[57].

Beyond the static view of snapshot experiments, there have been several great attempts to reconstruct the temporal evolution of ENSO using continuous or quasi-continuous transient model simulations. These range from early pioneering work employing an ENSO model of intermediate complexity[32,34], to coupled general circulation model (CGCM) forced solely by orbital variations[36], and more recently to CGCMs simulations incorporating increasingly realistic, time-evolving external forcings and boundary conditions[11,12,58]. Despite different model configurations and forcing designs, all these simulations reveal a dominant precessional control on overall ENSO variability strength, operating either through the "frequency entrainment" mechanism emphasized in earlier studies[32,34,36] or through changes in air–sea coupling strength in more recent work[11,12,58]. Greenhouse gas and ice-sheet forcings also influence ENSO during glacial–interglacial periods, likely through the "frequency-entrainment" mechanism, but their effects tend to intertwine and offset each other, adding complexity to the transient evolution of ENSO[11,12].

Although these previous transient simulations have provided valuable insights into past ENSO evolution, they extend at most to the last few glacial-interglacial cycles (~300 ka)[12]. ENSO evolution over earlier periods and longer timescales remains largely unknown, especially given that ENSO may have operated on Earth for at least 3 Ma[59,60]. Recently, Yun et al. [61] conducted an unprecedented transient simulation with the Community Earth System Model version 1.2 (CESM1.2), substantially extending the temporal scope of paleoclimate back to the past 3 Ma. The simulation incorporates multiple time-evolving external climate forcings while prescribing a fixed LGM ocean bathymetry. While their preliminary analyses suggest distinct variability features of the tropical Pacific climate, the detailed evolution of ENSO characteristics and the associated governing mechanisms remain unexplored. This gap motivates our further investigation of paleo-ENSO variability using this simulation.

In this study, we show that both the intensity and zonal position of ENSO variability are dominated by precession rather than by other external forcings, with pronounced responses emerging only under specific precession phases. We then conducted a mechanistic investigation emphasizing how precession-modulated interannual air–sea coupling processes and background states in the tropical Pacific (i.e., sea surface warming pattern and rainbands) govern changes in ENSO characteristics. Building on this dynamical understanding, we further examine the temporal evolution of ENSO characteristics and discuss the role of the gradually intensified background South Pacific Convergence Zone (SPCZ), driven by greenhouse gas and ice-sheet forcings, in mediating a progressively stronger precession–ENSO connection toward the present day.

Results

ENSO variability strength and zonal position

To identify the modulation of ENSO activity by external forcings, we characterize ENSO variability using the variance of interannual (<8-year) surface temperature (TS) anomalies computed within nominal 1000-year windows (i.e., millennial resolution), after correcting raw model outputs for "paleo calendar effect" (Methods). Owing to data limitations, TS, which is identical to SST over open oceans, is employed following previous studies[62,63]. The simulated ENSO activity remains persistently active with no apparent long-term trend (Supplementary Figs. 1a, b), despite the gradual global cooling over the full simulation period[61]. In both the eastern and central equatorial Pacific, ENSO variability exhibits pronounced fluctuations at precession timescales (~19–23 kyr), while variability at other orbital timescales is comparatively weak (Supplementary Figs. 1c, d). This is consistent with earlier work highlighting the dominant precessional control on tropical climate and ENSO activity[12,34,36,64]. Accordingly, our subsequent analyses focus primarily on the precessional modulation of ENSO.

To comprehensively reveal the impact of precession, we employ an asymmetric linear regression approach (Methods) and regress interannual TS variance onto normalized precession indices under their respective positive and negative phases (Fig. 1). Following previous studies[13,65–67], we adopt a pair of orthogonal precession indices, namely solstice and equinox precession indices (Methods), which respectively characterize the precession-induced seasonal contrast in TOA insolation between the two solstices and between the two equinoxes (Supplementary Fig. 2).

Under winter-solstice perihelion (i.e., maximums of solstice precession parameter, like the Late Holocene; hereafter, season refers to the Northern Hemisphere), interannual TS variance shows a clear basin-wide enhancement across much of the central and eastern equatorial Pacific, with only a minor reduction west of the dateline (Fig. 1a). In contrast, ENSO response is substantially weaker under the summer-solstice perihelion (Fig. 1b; minimums of solstice precession parameter). This illustrates a pronounced asymmetric precessional influence on ENSO strength. Quantitatively, interannual TS variance in the equatorial central-eastern Pacific (170°-90°W, 5°S-5°N) is approximately 4 times more sensitive to per unit of normalized precessional forcing under the winter solstice perihelion ($0.06K^2$) than under the summer solstice perihelion ($0.015K^2$), yielding a normalized asymmetry metric of 0.61 (Fig. 1c; Methods). Previous studies[12,34,36] have identified a similar role of solstice precession in ENSO intensity, though the asymmetry feature is less emphasized.

Beyond ENSO variability strength that has been the primary focus of most previous studies, we further identify an asymmetric modulation of the zonal position of central Pacific ENSO variability by equinox precession (Fig. 1d–f). When perihelion occurs near the vernal equinox (Fig. 1d; maximums of equinox precession parameter), the central Pacific ENSO action center moves eastward, producing a zonal dipole pattern with enhanced variability in the eastern central Pacific (160°–130°W, 5°S–5°N) and reduced variability in the western central Pacific (160°E–170°W, 5°S–5°N). In contrast, such a zonal dipolar change is far less evident under the autumn-equinox perihelion (Fig. 1e; minimums of equinox precession parameter). Quantitatively, the zonal dipole TS variance index is 4.6 times more sensitive to the normalized precessional forcing under the vernal-

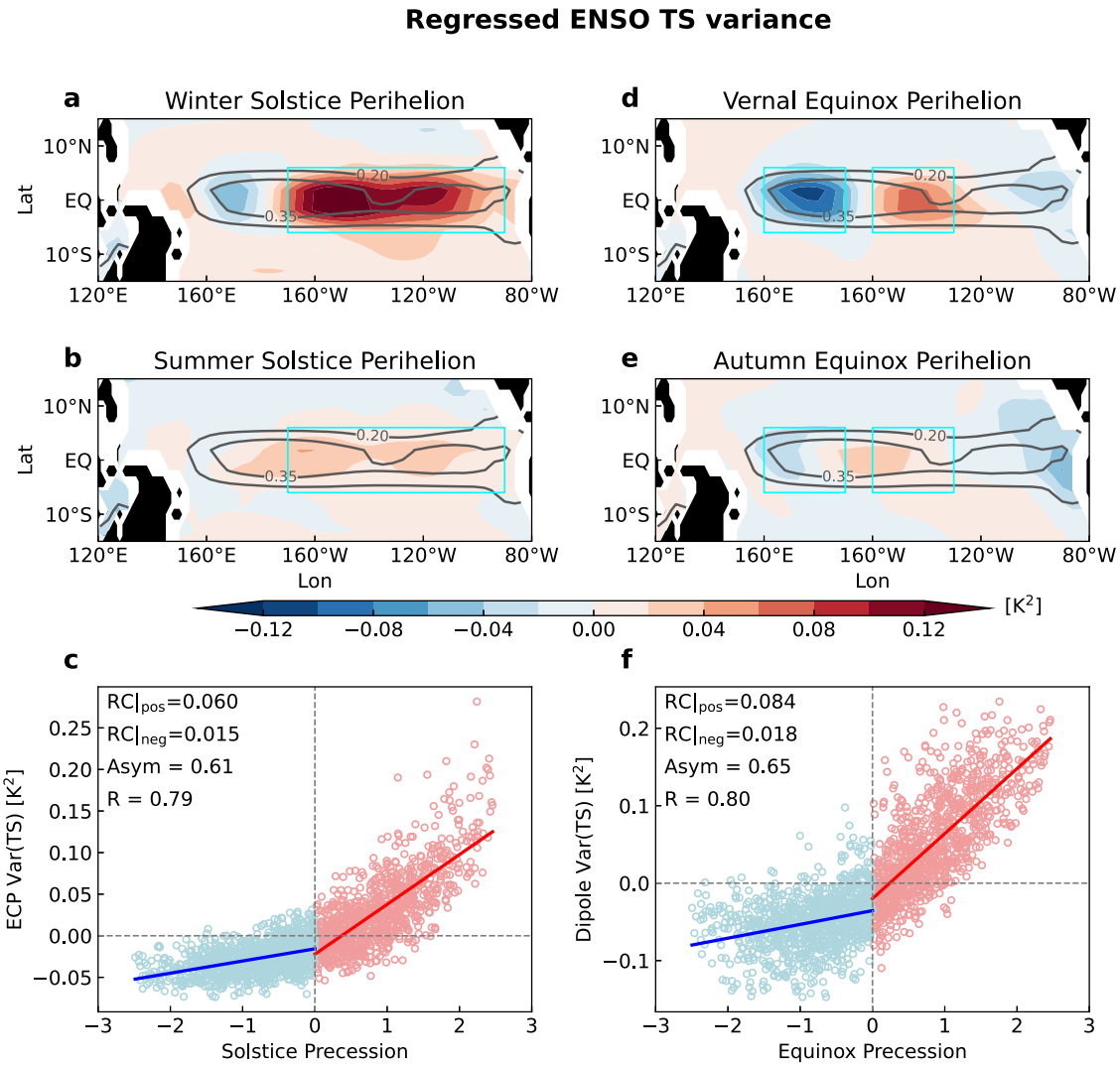


Fig. 1 | Asymmetric modulation of ENSO variability by two precession signals. Regressed patterns of ENSO TS variance (shading; K^2) onto (**a**) positive (winter-solstice perihelion) and (**b**) negative (summer-solstice perihelion) phases of the normalized solstice precession index. Contours show the long-term mean ENSO TS variance (units: K^2). (**c**) Scatter plot between the normalized solstice precession index and the ENSO TS variance index over the central-eastern equatorial Pacific (170°–90°W, 5°S–5°N). The asymmetric regression slopes for the two phases (RC|pos and RC|neg), the corresponding normalized asymmetry metric (Asym; Eq. (2) in Methods), and the correlation coefficient (R) are annotated. Because the spatial influences of solstice and equinox precession partially overlap, the contribution of equinox precession is removed when calculating the TS variance index. This is accomplished by subtracting the reconstructed ENSO TS variance associated with the equinox precession index, obtained using the asymmetric linear regression framework (Eq. (3) in Methods). (**d**) and (**e**) are similar to (**a**) and (**b**), but show regressed ENSO TS variance patterns associated with the positive (vernal-equinox perihelion) and negative (autumn-equinox perihelion) phases of the normalized equinox precession index. **f** As in (**c**), but for the relationship between the normalized equinox precession index and the zonal differences in ENSO TS variance between the eastern (160°–130°W, 5°S–5°N) and western–central Pacific (160°E–170°W, 5°S–5°N). Here, the influence of solstice precession is similarly regressed out when constructing the zonal-dipole TS variance index (Eq. (3) in Methods). All data are at millennial resolution and span the past 2 Ma due to data limitations (Methods).

equinox perihelion (0.084 K^2) than under the autumn-equinox perihelion (0.018 K^2), yielding a normalized asymmetry metric of 0.65 (Fig. 1f).

ENSO air-sea coupling processes

In this section, we analyze interannual ocean-atmosphere coupling processes associated with ENSO to gain insights into the asymmetric precessional modulation of ENSO characteristics. ENSO development involves a suite of coupled feedbacks arising from interactions among SST anomalies, the overlying atmosphere, and the upper-ocean dynamics in the tropical Pacific. During El Niño episodes, surface warming in the central-eastern equatorial Pacific enhances atmospheric convection and induces westerly wind anomalies over the central–western equatorial Pacific. These westerly wind anomalies change ocean dynamic fields, including a deepened thermocline in the eastern Pacific and eastward surface current anomalies, that amplify the initial surface warming anomalies through thermocline feedback and zonal advective feedback[68–70]. Meanwhile, intensified atmospheric convection increases cloudiness, which damps surface warming anomalies by reducing net surface heat flux. Thus, precessional modulation of ENSO characteristics can be understood from its influences on these major air-sea coupling processes.

Figure 2 presents the long-term mean and the solstice precession-modulated ENSO coupling sensitivities. As an illustrative example, ENSO precipitation sensitivity quantifies the anomalous precipitation response to a unit ENSO TS anomaly. It is estimated by regressing interannual precipitation anomalies onto an ENSO TS index defined over the central–eastern equatorial Pacific (160°E–90°W, 5°S–5°N) within each nominal 1000-year window. Larger precipitation sensitivity indicates that ENSO-related interannual surface warming anomalies more effectively induce precipitation responses. Analogous calculations and interpretations are applied to other ENSO-related variables, including TS, zonal wind stress,

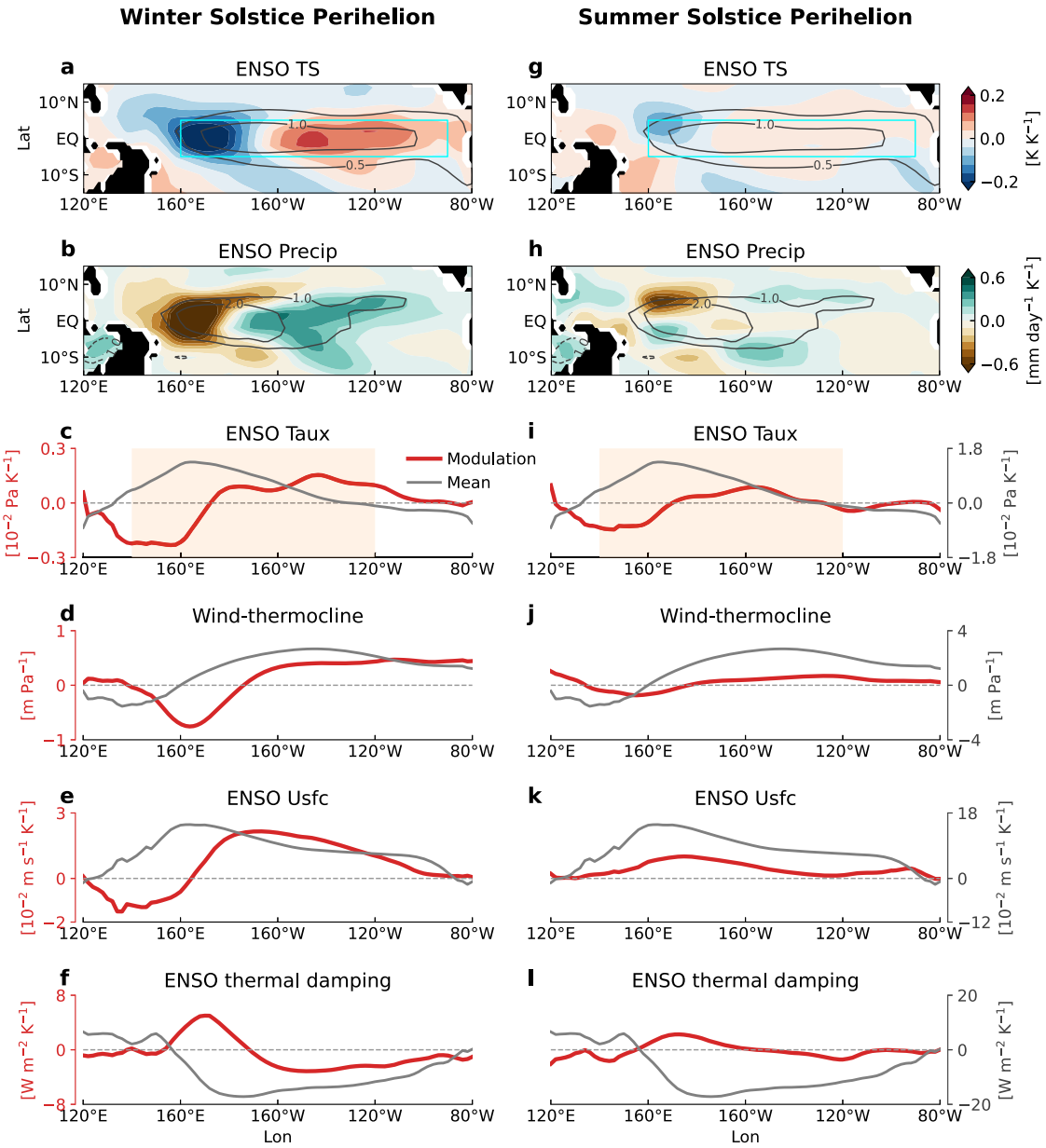


Fig. 2 | Asymmetric modulation of ENSO air-sea coupling sensitivities by solstice precession. Regressed coupling sensitivities of (**a**) ENSO TS (shading; K K^{-1}), (**b**) ENSO precipitation (shading; mm day^{-1} K^{-1}), (**c**) ENSO surface zonal wind stress (red line; 10^{-2} Pa K^{-1}), (**d**) thermocline to zonal wind stress (red line; m Pa^{-1}), (**e**) ENSO surface zonal current (red line; 10^{-2} m s^{-1} K^{-1}), and **f** ENSO net surface heat flux (red line; positive downward; W m^{-2} K^{-1}) onto the positive phase of the normalized solstice precession index (winter-solstice perihelion). Contours and gray lines denote the corresponding long-term means. **g**–**l** are the same as (**a**–**f**), but for the negative phase of the normalized solstice precession index (summer-solstice perihelion). ENSO sensitivity at millennial resolution is computed by regressing each variable's interannual (<8-year) anomalies onto the ENSO TS index over the equatorial central–eastern Pacific (160°E–90°W, 5°S–5°N; box in (**a**)) in each nominal 1000-year window. Wind–thermocline coupling sensitivity is diagnosed by regressing equatorial sea-surface-height anomalies onto zonal wind stress anomalies over the central–western equatorial Pacific (140°E–120°W, 5°S–5°N; orange shading in (**c**)). All data are at millennial resolution and span the past 2 Ma due to data limitations (Methods).

zonal ocean surface current, and net surface heat flux (i.e., thermal damping). We also diagnose the wind-thermocline coupling sensitivity, a key component of the thermocline feedback, by regressing sea surface height anomalies onto zonal wind stress anomalies in the central–western Pacific (140°E–120°W, 5°S–5°N). This metric has a dynamical basis in the quasi-balance between upper-ocean zonal pressure gradients and zonal wind stress[71–74]. After deriving all coupling sensitivities at millennial resolution, we take their long-term means as reference states and examine their responses to precession forcing using the asymmetric linear regression approach (Methods).

Compared with the reference states (gray contours and lines in Fig. 2), the ENSO air–sea coupling center intensifies and shifts eastward under the winter-solstice perihelion (shading and red lines in Fig. 2a–f). This eastward shift is evident in the enhanced TS and precipitation sensitivities in the eastern equatorial Pacific and the weakening west of the dateline (Fig. 2a, b). Notably, in the eastern Pacific, the precession-induced increase in precipitation sensitivity extends toward off-equatorial regions, aligning with the climatological Intertropical Convergence Zone (ITCZ) and SPCZ rainbands. This pattern is reminiscent of extreme El Niño conditions[75–78], in which strong eastern Pacific warming anomaly diminishes the meridional temperature gradient, draws the climatological rainbands equatorward, and thus produces massive near-equatorial precipitation anomalies. Consistent with the precipitation and TS sensitivity changes, the equatorial zonal wind stress sensitivity also intensifies and shifts eastward (Fig. 2c), leading to

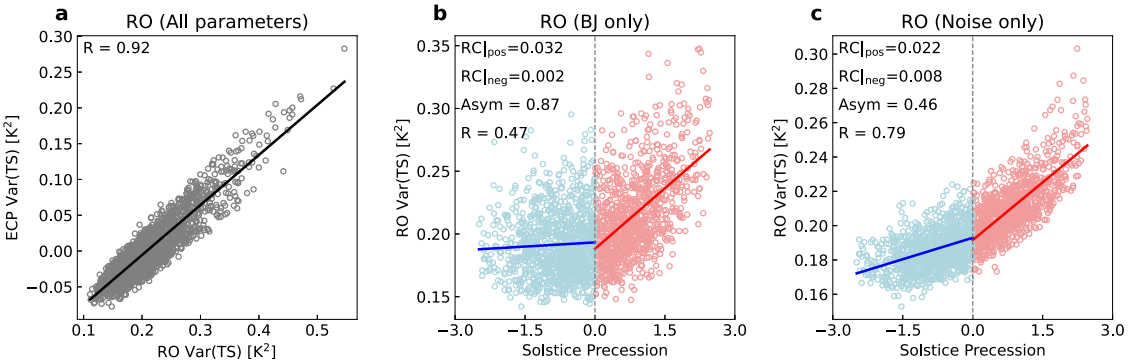


Fig. 3 | Asymmetric modulation of ENSO variability strength by solstice precession in the recharge oscillator (RO) model. a Scatter plot comparing ENSO TS variance (K^2) over the central–eastern equatorial Pacific (170°–90°W, 5°S–5°N) from the CESM1.2 simulation (y-axis) with that simulated by the RO model (x-axis), in experiments where all model parameters are allowed to vary. **b** Scatter plot between the normalized solstice precession index and the simulated ENSO TS variance in the RO model when only the Bjerknes feedback parameters vary, while all other model parameters are fixed at their long-term means. **c** As in (**b**), but for RO simulations in which only the noise-related parameters are allowed to vary. The asymmetric regression slopes for the two precession phases (RC|pos and RC|neg), the corresponding normalized asymmetry metric (Asym), and the correlation coefficient (R) are indicated. The RO model is configured by coupling interannual equatorial Pacific sea-surface-height anomalies (120°E–80°W, 5°S–5°N) with Niño 3 (150°–90°W, 5°S–5°N) TS anomalies. All data are at millennial resolution and span the past 2 Ma due to data limitations (Methods).

greater thermocline deepening in the eastern Pacific, as indicated by local positive sea surface height anomalies, and stronger eastward surface current anomalies (Fig. 2d, e). Both processes enhance ENSO growth in the eastern Pacific through intensifying thermocline and zonal advective feedbacks. The eastward displacement of the ENSO air–sea coupling is consistently reflected in the thermal damping term (Fig. 2f), where reduced shortwave radiation anomalies owing to increased convection-induced cloudiness likely play a dominant role[70].

In contrast, under summer-solstice perihelion, the precessional modulation of coupling sensitivities becomes much less pronounced (shading and red lines in Fig. 2g–l). Changes in TS sensitivity are negligible (Fig. 2g), and only weak, spatially scattered changes emerge in precipitation sensitivity over the off-equatorial regions (Fig. 2h). The resulting weak change in zonal wind stress sensitivity is insufficient to induce substantial thermocline adjustments or strong ocean surface currents (Fig. 2i–k), thereby inhibiting significant ENSO development. A similarly weak response is also evident in the thermal damping (Fig. 2l). Altogether, the stark contrast in ENSO air-sea coupling sensitivities between the two solstice perihelion suggests that they may be essential in the asymmetric precessional modulation of ENSO variability strength.

As a further verification, we employ the theoretical Recharge Oscillator (RO) model by coupling Niño3 (150°W–90°W, 5°S–5°N) TS anomalies with equatorial Pacific (120°E–80°W, 5°S–5°N) sea surface height anomalies (Methods). RO model parameters are first estimated within each nominal 1000-year window, and stochastic simulations are then conducted using either (i) the window-specific parameters (i.e., retaining temporal variations and precessional modulation) or (ii) the long-term mean parameters across all windows (i.e., without temporal changes or precessional modulation). This experimental framework enables us to isolate the processes responsible for the asymmetric precessional modulation of ENSO variability. When all parameters are allowed to vary temporally, the RO-simulated TS variability scales linearly and closely with the central–eastern Pacific TS variance from CESM1.2 (R = 0.92; Fig. 3a), confirming the good performance of the RO model. When only temporal variations in the Bjerknes-feedback parameters representing air-sea coupling processes are retained while all other parameters are fixed at their long-term means, the RO model successfully reproduces the asymmetric sensitivity of TS variance to the solstice precession index (Fig. 3b). The RO-simulated TS variance is roughly 16 times more sensitive to a unit of normalized precessional forcing under the winter-solstice perihelion (0.032 K^2) than under the summer-solstice perihelion (0.002 K^2; Fig. 3b). This corresponds to a normalized asymmetry metric (Methods) of 0.87, about 40% stronger than the asymmetry found in the CESM1.2 simulations (0.61; Fig. 1c). In contrast, when only temporal variations in stochastic forcing are retained (Fig. 3c), the asymmetric precessional modulation becomes much weaker, resulting in an asymmetry metric of 0.49, smaller than the CESM1.2 value (Fig. 1c). In brief, our RO results indicate that air–sea coupling processes play the dominant role in producing the asymmetric precessional modulation of ENSO variability strength, whereas stochastic processes contribute secondarily.

Similarly, we next examine how equinox precession modulates the air–sea coupling sensitivities to understand its influences on the zonal displacement of the central-Pacific ENSO variability (Fig. 4). Under the vernal-equinox perihelion, ENSO air–sea coupling also modestly intensifies and shifts eastward relative to reference states (gray contours and lines in Fig. 4). The resulting zonal-dipole modulation pattern (shading in Fig. 4a, b), which is also evident under winter-solstice perihelion (shading in Fig. 2a, b), is likely mediated by changes in the local Walker circulation. Enhanced surface warming and atmospheric convection over the eastern central Pacific suppress precipitation sensitivity in the western Pacific through convective subsidence, and reduce TS sensitivity there likely via eastward detrainment of warm water with strengthened anomalous surface zonal winds and currents.

However, unlike the winter-solstice perihelion response (Fig. 2a), the enhancement of TS sensitivity under vernal-equinox perihelion is largely confined to the central Pacific west of ~120°W, with little strengthening in the far eastern Pacific (Fig. 4a). Consequently, the associated increase in precipitation sensitivity (Fig. 4b) is concentrated in the eastern portion of the central Pacific and remains largely confined to the equator, showing limited alignment with the off-equatorial rainbands. Compared with the winter-solstice perihelion case, the response is weaker both over the equatorial central Pacific and in the off-equatorial eastern Pacific near the ITCZ (Supplementary Fig. 3).

Therefore, the eastward extension of zonal wind stress sensitivity (Fig. 4c) becomes less pronounced than that under winter-solstice perihelion (Fig. 2c). The zonal-dipole changes in wind stress sensitivity over the central-western Pacific largely cancel each other, resulting in weakly negative changes in wind-thermocline sensitivity in the eastern Pacific (Fig. 4d) and thereby limiting the changes of thermocline feedback. Instead, the eastward shift of ENSO is more related to the zonal advective process, as evidenced by the similarly displaced surface zonal-current sensitivity (Fig. 4e). Strengthened eastward current anomalies in the eastern central Pacific transport warmer climatological waters from the west, promoting local TS anomaly growth. This resembles the dynamics of central Pacific El Niño events, in which zonal advection feedback plays a critical role[69,79,80].

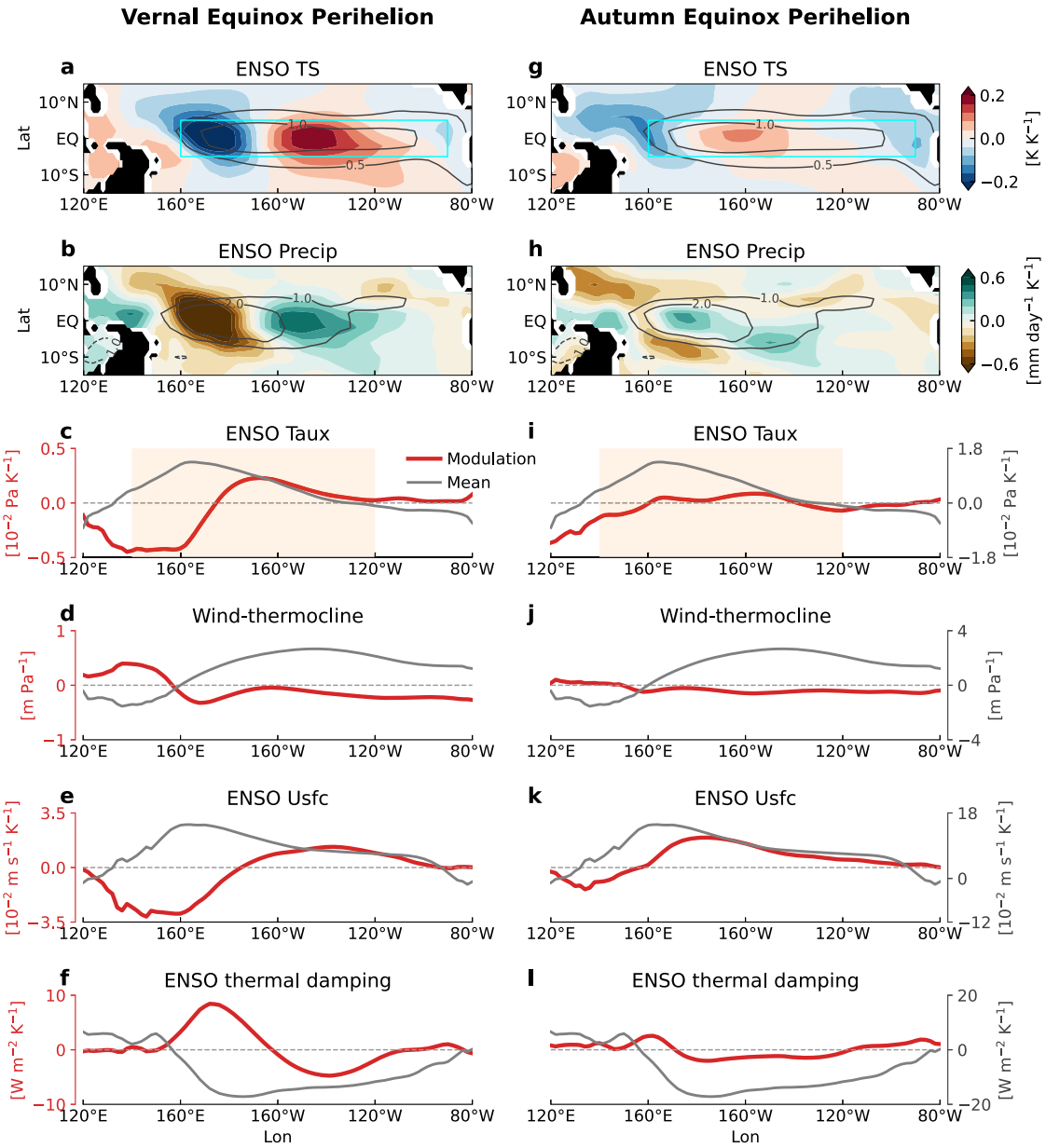


Fig. 4 | Asymmetric modulation of ENSO air-sea coupling sensitivities by equinox precession. Regressed coupling sensitivities of (**a**) ENSO TS (shading; K K^{-1}), **b** ENSO precipitation (shading; mm day^{-1} K^{-1}), **c** ENSO surface zonal wind stress (red line; 10^{-2} Pa K^{-1}), **d** thermocline to zonal wind stress (red line; m Pa^{-1}), (**e**) ENSO surface zonal current (red line; 10^{-2} m s^{-1} K^{-1}), and **f** ENSO net surface heat flux (red line; positive downward; W m^{-2} K^{-1}) onto the positive phase of the normalized equinox precession index (vernal-equinox perihelion). Contours and gray lines denote the corresponding long-term means. **g–l** are the same as (**a–f**), but for the negative phase of the normalized equinox precession index (autumn-equinox perihelion). ENSO sensitivity at millennial resolution is computed by regressing each variable's interannual (<8-year) anomalies onto the ENSO TS index over the equatorial central–eastern Pacific (160°E–90°W, 5°S–5°N; box in (**a**)) in each nominal 1000-year window. Wind–thermocline coupling sensitivity is diagnosed by regressing equatorial sea-surface-height anomalies onto zonal wind stress anomalies over the central–western equatorial Pacific (140°E–120°W, 5°S–5°N; orange shading in (**c**)). All data are at millennial resolution and span the past 2 Ma due to data limitations (Methods).

Consistent with the eastward-shifted ENSO precipitation sensitivity, the precessional modulation of the thermal damping sensitivity also shifts eastward and acts as a negative feedback counteracting ENSO TS sensitivity changes (Fig. 4a, f).

In contrast, when perihelion occurs near the autumn equinox, the modulation of TS sensitivity becomes substantially weaker and is displaced westward relative to that under the vernal-equinox perihelion, with the enhancement centered near 160°W (Fig. 4a, g). The precipitation response is spatially less organized, and all associated air–sea coupling processes weaken accordingly (Fig. 4h–l). Together with the results under the vernal-equinox perihelion (Fig. 4a–f), this reveals a pronounced asymmetric modulation of ENSO air–sea coupling sensitivities by equinox precession (Fig. 1d–f). Because the thermocline process plays a less important role in the eastward shift of ENSO (Fig. 4d, j), the RO model framework is not applicable to interpret the ENSO center shifts.

Basic states

The precessional modulation of ENSO variability magnitude and longitudinal position can be attributed to changes in the tropical Pacific background state, particularly the sea surface warming pattern and the associated distribution of ITCZ and SPCZ rainbands, which are also subject to evident precessional modulation. To characterize the spatial pattern of surface

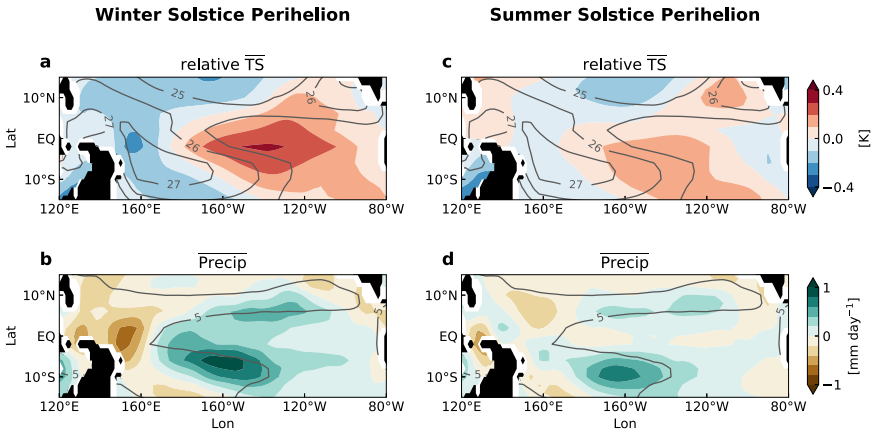


Fig. 5 | Asymmetric modulation of tropical Pacific mean states by solstice precession. Regressed patterns of annual-mean (**a**) relative TS (shading, K), and (**b**) precipitation (shading, mm day^{-1}) onto the positive phase of the normalized solstice precession index (winter-solstice perihelion). Contours denote the long-term means of (**a**) TS and (**b**) precipitation. **c** and (**d**) are the same as (**a**) and (**b**), respectively, but for the negative phase of the normalized solstice precession index (summer-solstice perihelion). Relative TS is defined as the local TS departure from the mean TS over global tropical oceans (0°–360°E, 20°S–20°N). All data are at millennial resolution and span the past 2 Ma due to data limitations (Methods).

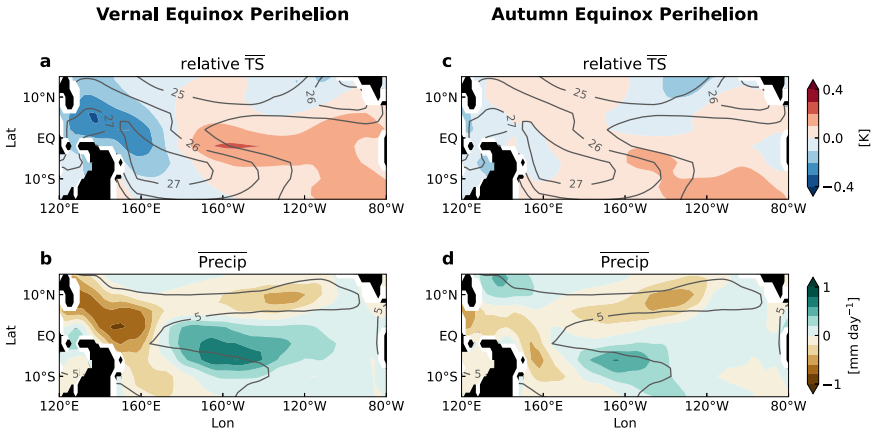


Fig. 6 | Asymmetric modulation of tropical Pacific mean states by equinox precession. Regressed patterns of annual-mean **a** relative TS (shading, K), and **b** precipitation (shading, mm day^{-1}) onto the positive phase of the normalized equinox precession index (vernal-equinox perihelion). Contours denote the long-term means of (**a**) TS and (**b**) precipitation. (**c**) and (**d**) are the same as (**a**) and (**b**), respectively, but for the negative phase of the normalized equinox precession index (autumn-equinox perihelion). Relative TS is defined as the local TS departure from the mean TS over global tropical oceans (0°–360°E, 20°S–20°N). All data are at millennial resolution and span the past 2 Ma due to data limitations (Methods).

warming, we adopt a relative TS metric by subtracting the mean TS over global tropical oceans (20°S–20°N, 0°–360°E) from the local TS. Compared to absolute surface temperature, this relative measure is more physically relevant for driving atmospheric circulation[81–85] and is especially suitable in our transient simulation, as it largely removes the mean tropical warming associated with CO_2 forcing (R = 0.96; Supplementary Fig. 4) and isolates the precession-induced TS signals.

Figure 5 presents the regressed annual-mean relative TS and total precipitation onto the normalized solstice precession index under its two phases. Under winter-solstice perihelion, a broad El Niño-like surface warming pattern emerges over the central-eastern tropical Pacific, accompanied by enhanced moistening in the tropical central Pacific, particularly along the off-equatorial SPCZ and ITCZ regions (Fig. 5a, b). This El Niño-like mean-state warming and the associated near-equatorial moistening destabilize the ocean-atmosphere coupled system, enabling interannual ENSO-related surface warming anomalies to more efficiently trigger atmospheric convection (i.e., enhanced ENSO precipitation sensitivity), thereby promoting stronger ENSO variability over the central-eastern Pacific[10,75,78,86,87]. This pattern closely resembles that under greenhouse-warming scenarios, where an El Niño-like warming leads to projected increases in future ENSO amplitude[6,88,89]. In our case, the mean moistening of the tropical Pacific rainbands, measured as the averaged background precipitation over SPCZ (170°E–130°W, 12°S–0°) and ITCZ (160°–120°W, 2°–10°N) regions, is strongly correlated with the central-eastern Pacific ENSO variability strength (R = 0.8) throughout the simulation, highlighting their collective roles in modulating overall ENSO intensity. According to an early study[28], winter-solstice perihelion reduces summer TOA insolation over the Northern Hemisphere (Supplementary Fig. 2a) and consequently weakens the Asian summer monsoon. The resulting reduction in monsoon convection weakens the tropical Pacific easterly trades by weakening the mean Walker Circulation and initiates mean surface warming in the equatorial eastern Pacific. This surface warming is further amplified by positive ocean-atmosphere feedbacks, reaching to the El Niño-like mean-state response.

Around the summer-solstice perihelion (Fig. 5c, d), we observe similar basic state response patterns, corresponding to a La Niña–like cooling and a weakened tropical Pacific rainband that acts to suppress ENSO activity if the regression signs are reversed to represent actual changes. Nevertheless, these responses are substantially weaker, amounting to roughly one-third to one-half of those under winter-solstice perihelio,n depending on the region, thereby showing a pronounced asymmetry. For example, the central Pacific relative TS response to a unit change in the normalized precession index is approximately 0.3 K for winter-solstice perihelion but only about 0.1 K for summer-solstice perihelion (Fig. 5a, c). This asymmetry is akin to the amplitude asymmetry between interannual El Niño and La Niña events in modern observations, wherein El Niño SST anomalies tend to grow more strongly than La Niña due to nonlinear ocean–atmosphere feedbacks[70,90]. We therefore propose that similar nonlinear feedbacks operate on precession timescales and contribute to the asymmetric mean-state responses, though the detailed physical processes warrant further investigation. Such asymmetric background conditions facilitate an asymmetric precessional modulation on ENSO variability strength.

Next, we conduct similar analyses with the equinox precession index (Fig. 6). Around the vernal-equinox perihelion, an El Niño-like warming pattern also emerges over the equatorial central-eastern Pacific (Fig. 6a), but it is relatively weaker, more narrowly confined to the

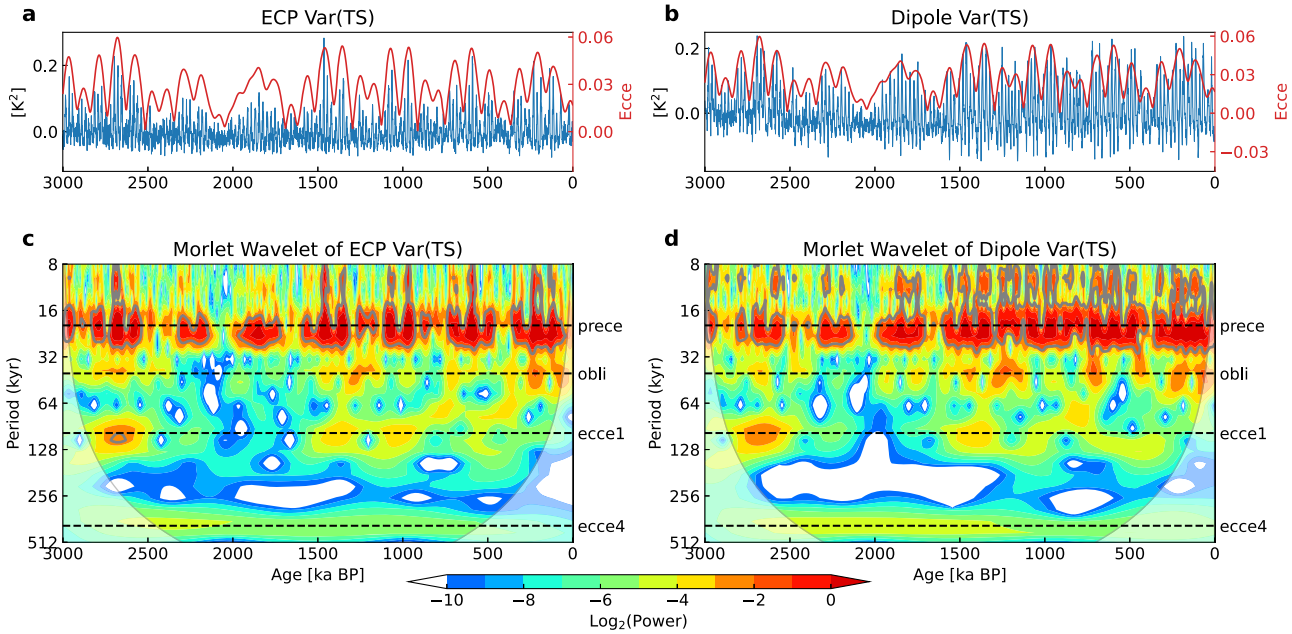


Fig. 7 | Temporal evolution of ENSO variability strength and zonal position. **a** Time series of the ENSO TS variance index over the central–eastern equatorial Pacific (170°–90°W, 5°S–5°N; blue; K²) and (**c**) its bias-rectified Morlet wavelet spectrum (shading) for the corresponding normalized index. **b** and (**d**) Same as (**a**) and (**c**), respectively, but for the zonal-dipole index, defined as the difference in ENSO TS variance between the eastern (160°–130°W, 5°S–5°N) and western–central Pacific (160°E–170°W, 5°S–5°N) regions. In (**a**) and (**b**), the orbital eccentricity index (red) is superimposed for comparison. In (**c**) and (**d**), gray contours mark regions of statistically significant wavelet power at the 90% confidence level based on an AR(1) red-noise null hypothesis. The parabola regions indicate the "cone of influence", where edge effects become important. Horizontal dashed lines mark the typical timescales associated with precession, obliquity, and eccentricity. All available 3 Ma data are used to provide the full temporal evolution of ENSO (Methods).

equator, and oriented more toward the Southern Hemisphere compared with that under winter-solstice perihelion (Fig. 5a). This warming pattern produces an interhemispheric thermal contrast that drives a meridional dipole precipitation response across the equator, with moistening in the south and drying in the north (Fig. 6b). The strengthened SPCZ promotes an intensification of ENSO precipitation sensitivity over the central-eastern Pacific[10,87], which outweighs the opposing influence associated with the weakened ITCZ, thereby enabling a modest eastward shift of central-Pacific ENSO variability. Because of these competing SPCZ and ITCZ effects, the ENSO amplitude in the far eastern Pacific exhibits minimal change (Fig. 1d; 4a). As a quantitative measure, the interhemispheric contrast in background precipitation, defined as the difference between area-averaged precipitation over the Southern Hemisphere (175°E–120°W, 0°-10°S) and the Northern Hemisphere (175°E–120°W, 5°–15°N), exhibits a strong correlation (R = 0.78) with zonal-dipole TS variance index, indicating its key role in controlling the zonal displacement of ENSO variability.

The contrasting annual-mean responses of SPCZ and ITCZ to equinox precession may stem from a nonlinear rectification of seasonal changes[13,36,91,92], considering the unique seasonality of the tropical eastern Pacific climate[93]. The equatorial cold tongue is typically warmest during boreal spring and coldest during boreal autumn, which is aided by wind–evaporation–SST feedback[93], favors a seasonally strengthened SPCZ in spring and an intensified ITCZ in autumn (Supplementary Fig. 5). The seasonally elevated background SST and moisture increase their sensitivity to insolation forcing, similar to the Asian monsoon case[28]. Under vernal-equinox perihelion, the enhanced springtime SPCZ resulting from increased TOA insolation outweighs its reduction during autumn under opposite insolation anomalies (Supplementary Fig. 2b), leading to an annual-mean net moistening of the SPCZ. Conversely, for the ITCZ, the annual-mean response is dominated by the insolation-induced weakening during autumn. These changes are further amplified by the tropical air-sea interactions toward the simulated patterns (Fig. 6a, b).

Similar mean-state response patterns are also found around the autumn-equinox perihelion (Fig. 6c, d), although they differ from those under the vernal-equinox perihelion in their detailed regional structures and response amplitudes (Fig. 6a, b). Specifically, the relative TS changes in the equatorial central Pacific are weaker and exhibit a greater emphasis in the off-equatorial Southern Hemisphere (Fig. 6c), resulting in a weaker SPCZ mean precipitation response (Fig. 6d). Consequently, the opposing rainband changes across the equator become comparable in magnitude, effectively cancelling each other's influences and resulting in a negligible net impact on air-sea coupling sensitivities and ENSO variability. As noted earlier, such asymmetries likely arise from nonlinear ocean-atmosphere feedbacks. In addition, the weak imprint of precession on CO_2 forcing may also provide a secondary contribution to the mean-state changes and their asymmetric expressions. Given the complexity of tropical air–sea interactions and multiple external forcings involved in this simulation, further investigation is needed to elucidate the roles of individual processes.

Time evolution

Having identified precessional modulations on ENSO characteristics through changing basic states and air-sea coupling processes in the tropical Pacific, we next examine their temporal variations to better comprehend past ENSO evolution in our simulation. Figure 7 shows the time series of interannual TS variance indices that represent ENSO variability magnitude and zonal displacement, along with the corresponding wavelet spectra of their normalized counterparts. Both time series show predominant precessional modulation, with the strongest wavelet power concentrated at the precession timescale (~19-23 kyr). Consequently, the upper envelopes of two ENSO TS variance indices closely track orbital eccentricity, the amplitude modulator of precession indices. In contrast, the lower envelopes remain nearly flat, indicating an asymmetric ENSO response to precession. This asymmetry gives rise to half-precession (~10 kyr) and weak eccentricity-band (~100 and ~400 kyr) wavelet power through nonlinear frequency cascading (Supplementary Note 1; Supplementary Fig. 6c).

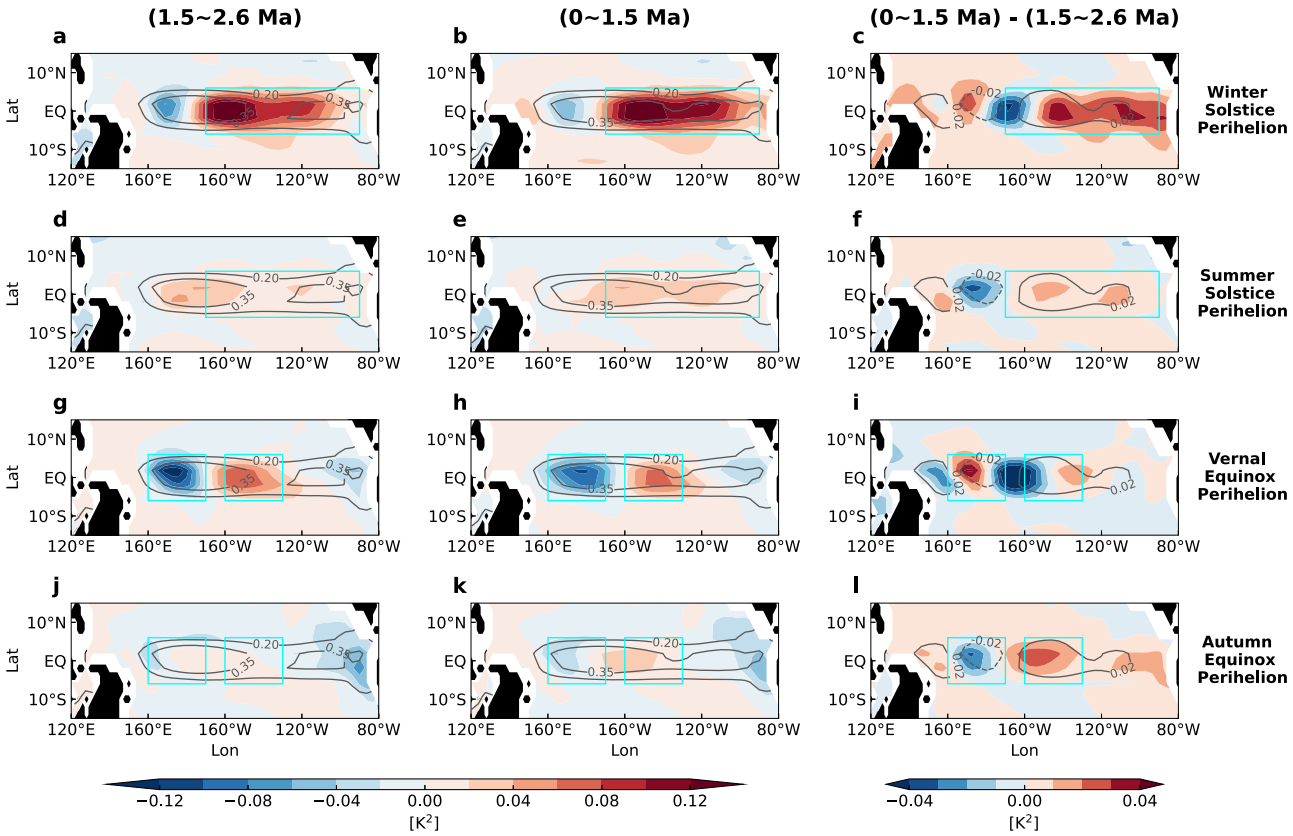


Fig. 8 | Differences in mean ENSO variability and its precessional modulation between the early and late Quaternary. Regressed patterns of ENSO TS variance (shading; units: K^2) onto the positive phase of the normalized solstice precession index (winter-solstice perihelion) during (**a**) the early Quaternary (1.5–2.6 Ma), (**b**) the late Quaternary (0–1.5 Ma), and (**c**) their difference. Contours denote the corresponding mean ENSO TS variance for each epoch and their difference. **d**–**f** are the same as (**a**–**c**), respectively, but for the negative phase of the normalized solstice precession index (summer-solstice perihelion). **g**–**l** follow the same format as (**a**–**f**), but for the positive (vernal-equinox perihelion; (**g**–**i**) and negative (autumn-equinox perihelion; **j**–**l**) phases of the normalized equinox precession index.

Although neither ENSO characteristic exhibits a clear long-term trend, notable differences remain across geological epochs. The modulation of the ENSO magnitude index undergoes an abrupt shift into a less active state at the onset of the Quaternary (~ 2.6Ma), remaining relatively quiescent until its reintensification after ~1.5 Ma (Fig. 7a). The transition at ~1.5 Ma appears earlier than the typical timing of Mid-Pleistocene Transition (MPT; 0.7-1.25 Ma)[17] and is more likely linked to a concurrent weakening of the 100-kyr component of orbital eccentricity, as suggested by their respective wavelet spectra (Fig. 7c; Supplementary Fig. 7). In addition, the sensitivity of ENSO magnitude to precessional forcing also appears diminished during the early half of the Quaternary (1.5–2.6 Ma). This is evidenced by a distinct gap between the upper envelope of the ENSO magnitude index and the eccentricity curve (Fig. 7a), as well as by the comparatively weak precession-scale wavelet power (Fig. 7c). Similar epochal differences are also identified in the ENSO zonal position index (Fig. 7b, d), whose precession-scale wavelet power strengthens progressively through the simulation and becomes more pronounced in the second half of the Quaternary (0-1.5 Ma).

To better illustrate the epochal differences, we compare the mean ENSO activity and its sensitivity to precessional forcing between the early (1.5–2.6 Ma) and second (0–1.5 Ma) half of the Quaternary (Fig. 8). While the overall ENSO characteristics and their precessional modulation remain broadly similar across the two epochs, the late Quaternary exhibits a modestly higher mean ENSO TS variance and stronger sensitivities to precessional forcing. The most pronounced difference appears under the winter-solstice perihelion (Fig. 8c), where the precession-modulated sensitivity of central–eastern Pacific ENSO strength is about 30% higher than in the early half of the Quaternary (Fig. 8a). In contrast, the intensification under the summer-solstice perihelion remains comparatively minor (Fig. 8f). Furthermore, equinox precession drives noticeably larger zonal shifts of the ENSO action center in the late Quaternary. Under vernal-equinox perihelion, the positive lobe of the TS variance center shifts eastward from ~150°W in the early half of the Quaternary to ~140°W in the second half of the Quaternary (Fig. 8g, h). Under autumn-equinox perihelion, the sensitivity of TS variance to precession forcing also strengthens in the central Pacific (Fig. 8j, k), producing a clearer zonal dipole change pattern (Fig. 8l).

Considering the pivotal role of relative TS over the central–eastern equatorial Pacific in shaping baseline ENSO activity and its precessional modulation, we next examine its temporal evolution and associated wavelet spectrum (Fig. 9). It is also dominated by precession-scale variability and displays epochal differences that are even more pronounced than those identified in the ENSO statistics (Fig. 7). Compared with the early half of the Quaternary, the second half of the Quaternary exhibits substantially larger precession-scale fluctuations in eastern-equatorial Pacific relative TS, indicating a stronger precessional modulation. Such stronger precession-induced background warming (or cooling) more effectively alters ENSO characteristics by modulating interannual air–sea coupling processes.

This raises an intriguing question: why do the equatorial basic states exhibit enhanced sensitivity to precessional forcing despite the overall global-mean cooling trend throughout the Quaternary? To explore this, we examine the difference maps of mean relative TS and precipitation between the two epochs in the tropical Pacific (Fig. 10a, b). Notably, the second half of the Quaternary features systematically higher relative TS and enhanced precipitation over the SPCZ region. This, together with the corresponding time series (Fig. 10c, d), indicates a gradual long-term intensification of the SPCZ. When the precession-induced basic-state changes, particularly the El Niño-like mean surface warming patterns under the winter-solstice or vernal-equinox perihelion (Figs. 5a, 6a), are superimposed on this gradually warming and moistening background, they can excite a stronger near-

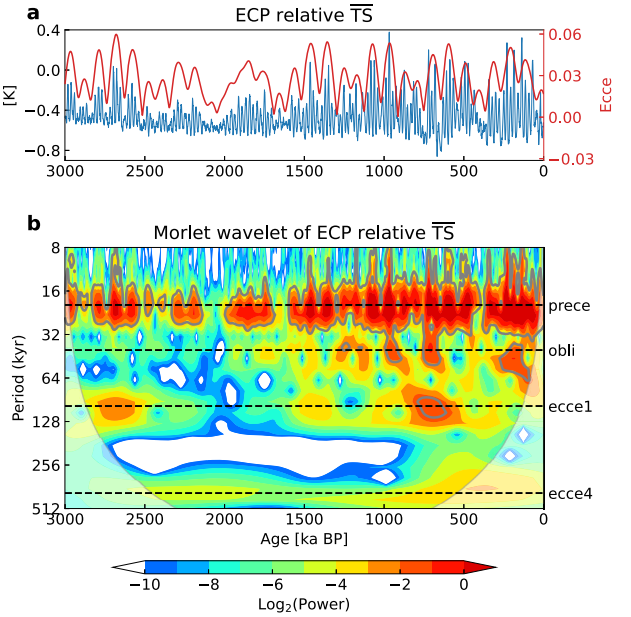


Fig. 9 | Temporal evolution of annual-mean relative TS over the equatorial central-eastern Pacific. **a**Time series of the annual-mean relative TS over the equatorial central-eastern Pacific (180°–90°W, 5°S–5°N; blue; K) and **b** its bias-rectified Morlet wavelet spectrum (shading) for the corresponding normalized index. The orbital eccentricity index (red) is superimposed in (**a**) for comparison. Gray contours in (**b**) mark regions of statistically significant wavelet power at the 90% confidence level based on an AR(1) red-noise null hypothesis. The parabola regions indicate the "cone of influence", where edge effects become important. Horizontal dashed lines mark the typical timescales associated with precession, obliquity, and eccentricity. All available 3 Ma TS data are used to provide the full temporal evolution (Methods).

equatorial mean-precipitation response similar to the interannual ENSO case. The resulting enhancement of tropical Pacific ocean–atmosphere coupling thus facilitates the stronger precession-modulated basic-state sensitivities in the second half of the Quaternary.

The long-term SPCZ trend is primarily attributed to greenhouse gas and ice-sheet forcings (Fig. 10e) associated with the gradual cooling of the Earth system. The progressive decrease in atmospheric CO_2 concentration (Fig. 10e) cools the Northern Hemisphere more strongly than the Southern Hemisphere, owing to the larger fraction of low-heat-capacity land surfaces in the north. The resulting interhemispheric energy imbalance[94] with a relatively warmer Southern Hemisphere promotes gradual warming and moistening over the SPCZ region (Fig. 10c, d). The prescribed Northern Hemisphere continental ice sheets (Fig. 10e) further amplify this interhemispheric energy imbalance through increased surface albedo and enhanced shortwave radiation deflection, an effect that becomes particularly pronounced after the MPT. This is evidenced by the stronger correlations between SPCZ background states (110°–170°W, 6°–14°S; enclosed boxes in Fig. 10a, b) and ice-sheet forcing (R = −0.63 for relative TS and R = −0.52 for precipitation) compared with those for CO_2 forcing (R = −0.44 for relative TS and R = −0.22 for precipitation) over the past 800 ka. Nevertheless, explicitly quantifying the relative contributions of CO_2 and ice-sheet forcing requires dedicated single-forcing simulations, which warrant further investigation to achieve a more complete understanding of tropical climate responses to external forcings.

To summarize, our analyses suggest that the abrupt reduction in ENSO activity during the early half of the Quaternary (Fig. 7a) is initiated by a concurrent weakening of orbital eccentricity. The contrast between this period and the late Quaternary was further amplified by the progressively stronger background modulation from the SPCZ, driven primarily by CO_2 and ice-sheet forcings. Prior to the Quaternary (2.6–3 Ma), persistently high eccentricity alone sustains relatively strong ENSO variability (Fig. 7a, b) and elevated relative TS in the equatorial eastern Pacific (Fig. 9a), despite a weak mean-state SPCZ (Fig. 10c, d). Together, these results highlight a complex interplay among multiple external forcings in producing abrupt shifts in the tropical climate system.

Given the central role of eccentricity in shaping past ENSO evolution, it is important to note that our simulation prescribes orbital parameters following the Berger (1978) solution[95], which deviates substantially from the more accurate astronomical solution of Laskar et al. [96] before around 1.5 Ma (Fig. 11). As such, the weakened eccentricity and associated simulated ENSO changes during the early Quaternary (1.5–2.6 Ma) may not have occurred in the real past, and any model–proxy comparisons prior to ~1.5 Ma should therefore be treated with caution. Nevertheless, our results provide valuable insights into the potential mechanisms governing past ENSO and tropical climate variability. Further simulations incorporating more accurate orbital solutions and refined external forcings will be essential for fully assessing these dynamics and their past evolution.

Discussion

In this study, we investigate key ENSO characteristics changes over the past 3 Ma using a newly developed transient coupled model simulation. Compared to previous studies that focused primarily on the solstice precessional modulation of ENSO variability strength[11,12,32,34], our results provide a more comprehensive picture of precession-ENSO relationship, by additionally identifying the role of equinox precession[13,65–67] in modulating the zonal position of central-Pacific ENSO variability and by explicitly elucidating the strong precession phase-dependency of ENSO responses (Fig. 12). Specifically, ENSO variability preferentially intensifies under winter-solstice perihelion, whereas central-Pacific ENSO activity moderately shifts eastward under vernal-equinox perihelion. We further demonstrate that interannual air-sea coupling processes, shaped by precession-modulated background surface warming patterns and the associated tropical rainbands, are essential for determining both ENSO characteristics changes. As such, the long-term envelope of ENSO largely tracks the orbital eccentricity. Meanwhile, the long-term intensification trend of the background SPCZ, following greenhouse gas and ice-sheet forcings, progressively amplifies precessional effects on ENSO toward the present day.

The nonlinear "frequency entrainment" mechanism have often been invoked in previous paleo-ENSO studies[32,34–36] to explain changes in ENSO variability strength through opposite responses of cold-tongue annual cycle amplitude. In our simulation, however, variations in the cold-tongue annual cycle amplitude are primarily modulated by equinox precession (R = 0.87; Supplementary Fig. 8), resulting in an approximately 90° phase shift relative to ENSO variability strength that is dominated by solstice precession[61]. Thus, the nonlinear "frequency entrainment" mechanism is not applicable to the precessional modulation of ENSO variability strength in our study. This is consistent with other transient simulation studies[11,12], which also emphasize the role of interannual air–sea coupling instability in ENSO intensity on precessional timescales. Given that precession strongly influences both ENSO characteristics[11,12,34] and the cold tongue seasonal cycle[67,97], their statistical relationship may primarily reflect a shared orbital forcing rather than a direct physical causality. Still, further in-depth investigations are needed to disentangle the intriguing relationship between ENSO variability strength and cold tongue seasonal cycle.

To contextualize our model results within previous paleo-ENSO studies[11,23–25,28–32,40,53,57,98], we examine ENSO variability during the mid-Holocene (~ 6 ka) and the LGM (~21 ka) by extracting interannual ENSO TS variance at 6 ka and 21 ka, respectively (Supplementary Fig. 9). Relative to the preindustrial simulation, the higher interannual TS variance at 6 ka indicates stronger ENSO variability (Supplementary Fig. 9a), seemingly at odds with earlier findings at first glance. Interestingly, however, the precession-related ENSO changes, reconstructed using our identified precession–ENSO relationship and past orbital parameters (Eqs. 3–4 in Methods), reveal a ~25% weakening of ENSO variability over the central–eastern equatorial Pacific, in much better agreement with prior modeling studies (cf. Lu and Liu, 2018 and references therein)[22]. This

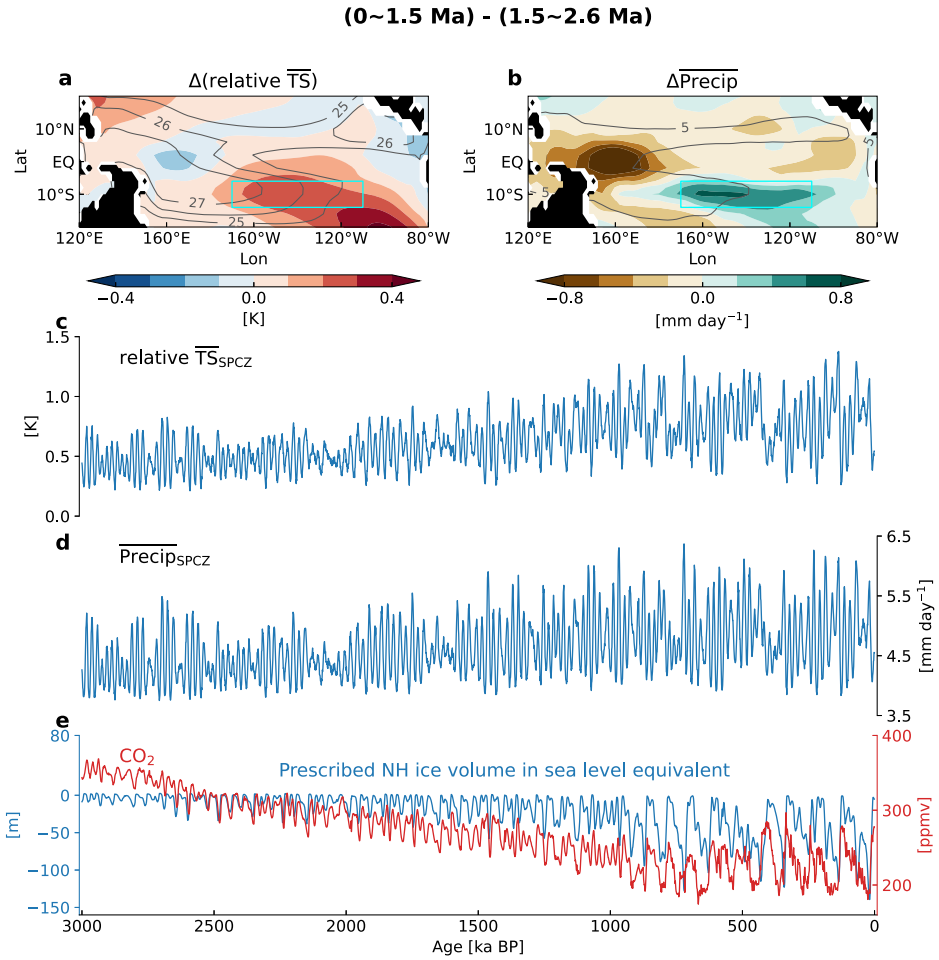


Fig. 10 | Long-term warming and moistening of the South Pacific Convergence Zone (SPCZ). **a** Difference in annual-mean relative TS (shading; K) between the early (1.5–2.6 Ma) and late (0–1.5 Ma) Quaternary. **b** Same as **a**, but for precipitation (shading; mm day^{-1}). Contours in (**a**) and (**b**) indicate the corresponding long-term mean TS and precipitation. Time series of annual-mean (**c**) relative TS (K) and (**d**) precipitation (mm day^{-1}) averaged over the SPCZ region (110°–170°W, 6°–14°S), as outlined in (**a**) and (**b**). **e** Time series of atmospheric CO_2 concentration (red; ppmv) and the prescribed Northern Hemisphere ice volume expressed as sea-level equivalent (blue; m). All available 3 Ma data are used to provide the full temporal evolution (Methods).

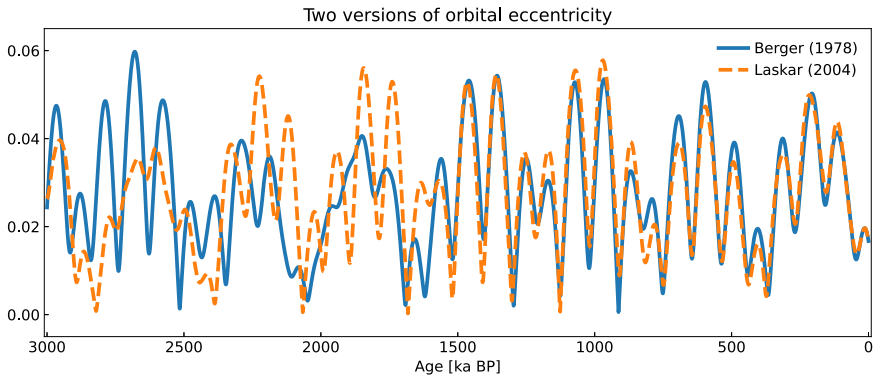


Fig. 11 | Comparison of two versions of orbital eccentricity. Time series of the orbital eccentricity used in CESM1.2 transient simulation, based on the solution of Berger (1978; blue solid)[95], and its counterpart from Laskar et al (2004; orange dashed)[96], shown over the past 3 Ma.

suggests that precession-induced ENSO changes in a single snapshot can be contaminated by other external forcings and internal climate variability (e.g., the Pacific Decadal Oscillation), particularly given a relatively weak precessional forcing during the Holocene than other geological periods (Supplementary Fig. 6a).

In contrast, ENSO variability during the LGM appears stronger than in the preindustrial period, with only minor contributions from precession (Supplementary Fig. 9d, e). The intensified ENSO is likely related to ice-sheet changes given pronounced changes in the sea surface warming pattern in the tropical Pacific (Supplementary Fig. 9f). The vast Northern Hemisphere continental ice sheets during LGM may amplify interhemispheric atmospheric energy contrasts through increased surface albedo, thereby inducing relative Southern Hemisphere warming, strengthening the SPCZ, and enhancing ENSO activity. Given the ongoing debate regarding ENSO behavior during the LGM[48], further efforts are needed to robustly constrain ENSO variability under cold climate states and to clarify its sensitivity to individual external forcings.

In addition to the asymmetric responses of tropical Pacific background states (i.e., mean surface warming pattern and rainbands) to precessional forcing, the asymmetric precessional modulation of ENSO characteristics also depends on our model's representation of ENSO. In the CESM1.2 piControl simulation, ENSO variability is weaker (~0.5 °C) and more westward-extended than observed, with two distinct ENSO action centers in the central and eastern equatorial Pacific (Supplementary Fig. 10). These discrepancies likely arise from coarse model resolution and common coupled-model biases[99] (e.g., cold tongue

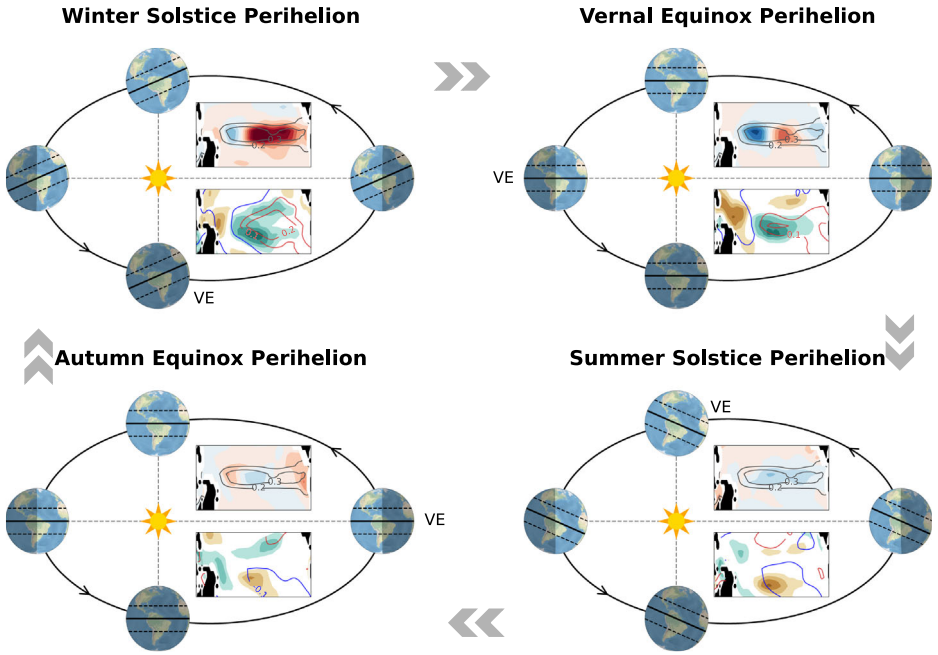


Fig. 12 | Schematic of asymmetric precessional modulation of ENSO and tropical Pacific mean states. Precession-induced modulation of ENSO TS variance (upper insets; shading; K^2) and the corresponding tropical Pacific mean states (lower insets) of relative TS (colored contours; K) and precipitation (shading; mm day^{-1}) under four representative precession configurations: winter-solstice perihelion, vernal-equinox perihelion, summer-solstice perihelion, and autumn-equinox perihelion. Contours in the upper insets denote the mean ENSO TS variance and serve as a reference. In the upper insets, red and blue shading indicate enhanced and reduced ENSO TS variance, respectively. In the lower insets, green and brown shading indicate increased and decreased annual-mean precipitation, while superimposed red and blue contours mark regions of enhanced and reduced annual-mean relative surface warming. "VE" denotes Earth's position at the vernal equinox in each subplot.

cooling bias) that weaken interannual air-sea coupling and limit ENSO growth, particularly in the eastern Pacific. Such model characteristics may inherently favor asymmetric ENSO responses to precessional forcing, as a relatively weak eastern-Pacific ENSO limits the extent of its further weakening, yet retains substantial potential for intensification under favorable warm background conditions (e.g., winter-solstice perihelion). Thus, our results may be model-dependent and further investigations using multiple models and more advanced model configurations are needed to achieve a more complete understanding of the precession-ENSO relationship and its past evolution.

Specifically, while our full 3 Ma transient simulation provides direct insight into long-term changes in the tropical Pacific background states (e.g., the SPCZ) and associated ENSO characteristics that are infeasible to assess using existing transient paleo-ENSO simulations, shorter transient simulations[12,67,100], which still encompass a sizeable number of precessional cycles, together with idealized precession phase-sliced experiments[97,101,102], remain well suited for elucidating precessional influences on tropical Pacific mean states, ENSO variability, and their asymmetric modulation. Accordingly, further intermodel comparison efforts would offer additional insights by clarifying model diversity and the underlying physical mechanisms, and will be pursued in future work.

Methods

Model configuration and experimental design

The quasi-continuous simulation over the past 3 million years was realized through the Community Earth System Model version 1.2 (CESM1.2)[103] under a computationally efficient configuration. CESM1.2 comprises the atmosphere (Community Atmosphere Model version 4, CAM4), ocean (Parallel Ocean Program version 2, POP2), sea ice (Community Ice Code version 4, CICE4), and land models (Community Land Model version 4, CLM4). The atmospheric and land components are configured with about 3.75° horizontal resolution (T31) and 26 vertical hybrid layers. The ocean model has 25 vertical levels, with a longitudinal resolution of about 3.6° and variable latitudinal resolution that approaches finer to ~0.9° near the equator (gx3v5, 100 × 116 horizontal grids). Despite the relatively coarse resolution, this model setup captures key features of tropical air–sea interactions and ENSO variability[11,92,99]. Similar configurations have been extensively used in previous paleoclimate studies[11,12,67,104].

To generate initial and restart files for the 3 Ma simulation, CESM1.2 was first integrated for 2300 model years under fixed preindustrial forcing. The first 1000 years are treated as a spin-up period, and only the remaining 1300 years are used in the analysis. The 3 Ma transient simulation incorporates several time-evolving external climate forcings, including orbital parameters, greenhouse gas concentrations, and continental ice-sheet changes.

Orbital forcing alters the seasonal and latitudinal distribution of TOA insolation and is governed by three key orbital parameters (i.e., precession, obliquity, and eccentricity), whose past evolution is derived from the analytical solution of Berger[95]. However, this solution becomes less accurate beyond around 1.5 Ma compared to the numerical solution later derived by Laskar et al. [96] (Fig. 11).

Greenhouse gas forcing, including CO_2, CH_4, and N_2O, affects the TOA radiative balance, and is accurately known only for the past ~800 ka years based on air-bubble measurements from Antarctic ice cores[105]. Prior to this, CO_2 concentrations are taken from a transient simulation[106] using an intermediate-complexity Earth system model CLIMBER-2 with interactive carbon cycle, while CH_4 and N_2O are roughly estimated using a global benthic $\delta^{18}O$ stack[107] and their empirical linear relationships since 800 ka. To compensate for the relatively low climate sensitivity of CESM1.2 and the possible indirect role of unresolved dust forcing, greenhouse gas anomalies relative to preindustrial levels are further amplified by a factor of 1.5.

The prescribed Northern Hemisphere ice sheets are also derived from the CLIMBER-2 simulation, while those in the Southern Hemisphere are held constant at preindustrial levels. The ice sheets primarily affect surface albedo and topography, with associated meltwater discharge omitted. We note this treatment as a caveat, as it likely underestimates the strength of the Atlantic Meridional Overturning Circulation and its influence on the tropical Pacific climate[108].

Following a 5-fold acceleration technique, all forcings (e.g., orbital parameters) are held fixed for every 20-model years (one super-model year), and then updated every 100 orbital years at the end of each 20-year model period. Thus, the 3 Ma simulation essentially yields a total of 600,000 model years. This relatively small acceleration factor is considered less influential on the interannual ENSO phenomenon of our interest, as ENSO typically involves upper-ocean feedbacks within the top few hundred meters, which have much shorter adjustment timescales compared to a complete precession cycle experienced by the model (~4000 model years).

Additionally, we employ a fixed LGM ocean bathymetry and land-sea mask based on ICE-6G_C data[109], in which key oceanic passages connecting the tropical Pacific and Indian Oceans (e.g., the Indonesian Throughflow) remain open (Supplementary Fig. 11), permitting present-day–like exchanges of water mass and energy between the two basins. This simplified treatment represents a generally reasonable approximation, given that the tropical land–sea configuration over the past ~3 Ma has remained broadly similar to the modern state, with no major tectonic reorganization. Nevertheless, some model biases are inevitable. In particular, the fixed LGM ocean bathymetry likely overestimates the exposure of the Sunda and Sahul shelves for much of the simulation, favoring a more positive Indian Ocean Dipole–like mean state and slightly enhanced mean convection over the tropical western Pacific[110]. These mean-state biases may partly contribute to an overestimation of mean ENSO variability in the central-western Pacific (Supplementary Fig. 10). Moreover, the absence of dynamical coastline modulation during the late Quaternary likely leads to an underrepresentation of associated perturbations in Indo–western Pacific climate mean states[110], inter-basin interactions[111], and their impacts on ENSO variability. This, together with the neglected effects of meltwater discharge, may underestimate the ENSO modulation on ice-sheet forcing timescales (~100 kyr) during the late Quaternary. Beyond the overview presented here, further experimental details and a comprehensive discussion of the limitations of this 3 Ma simulation can be found in Yun et al. [61].

Physical variables, calendar adjustment, and ENSO statistics

Because of storage constraints, only a subset of monthly surface climate variables is archived in the ICCP climate data server (Supplementary Table 1). Specifically, monthly surface temperature (TS) and total precipitation (PRECT) are available for the full 3 Ma simulation, whereas other fields, such as TOA insolation (SOLIN) and zonal wind stress (TAUX), are archived only for the most recent 2 Ma. To maximize the utility of the dataset, our mechanistic analysis of precessional modulation of ENSO (Figs. 1–6) is based on the 2 Ma period for which all relevant dynamical variables are available, ensuring analysis consistency. Building on this dynamical understanding, we then extend our analysis to the full 3 Ma data to provide the long-term evolution of ENSO variability and the associated changes in key background states (Figs. 7–11). To compare the simulated ENSO variability with that of the modern climate, we also analyzed monthly SST from 1979 to 2024 using the Extended Reconstructed Sea Surface Temperature version 5 (ERSSTv5) reanalysis[112].

To account for the "paleo calendar effect"[113] arising from changes in month length under different orbital configurations, we first converted original CESM1.2 monthly outputs from a fixed-length calendar ("365d_calendar") to a fixed-angular calendar[114] for each 20 model-year simulation under identical external forcings (i.e., one super-model year). On this basis, we grouped the full 600,000 model years into 3000 chunks, each containing 10 super-model years (i.e., 200 model years), and computed ENSO statistics and tropical Pacific mean states within each chunk. This procedure yields nominal millennial-resolution characteristics considering the aforementioned 5-fold acceleration simulation technique.

The annual-mean climatology of the relevant climate variables within each chunk is treated as the background state. ENSO-related interannual anomalies were obtained by first removing the chunk-specific seasonal climatology of each variable, followed by applying an 8-year high-pass Lanczos filter[115] to minimize potential interference from lower-frequency climate variability (e.g., the Pacific Decadal Oscillation). The millennial-resolution ENSO activity is then quantified as the variance of interannual TS anomalies within each chunk. Likewise, the millennial-resolution ENSO-associated coupling sensitivities were computed by regressing each physical variable (e.g., TS, precipitation, wind stress) onto the ENSO TS index over its main action center in the central–eastern Pacific (160°E–90°W, 5°S–5°N) within each chunk (i.e., 10 super-model years). The wind–thermocline coupling sensitivity is similarly diagnosed within each chunk by regressing equatorial sea-surface-height anomalies onto zonal wind stress anomalies over the central–western equatorial Pacific (140°E–120°W, 5°S–5°N).

Asymmetric linear regression and reconstruction

In this study, we quantify the precessional modulation of millennial-resolution ENSO characteristics and background states using an asymmetric linear regression approach[70,116]:

$$F = \begin{cases} \alpha_{pos} \times p + \beta_{pos} \left(p > 0\right) \\ \alpha_{neg} \times p + \beta_{neg} \left(p < 0\right) \end{cases} \tag{1}$$

where p is either the solstice or equinox precession index. Here, α denotes the regression slope (i.e., the sensitivity to precession forcing), and β is the regression intercept. The subscripts "pos" and "neg" indicate results obtained under positive and negative phases of each precession index, respectively. F represents the millennial-resolution ENSO statistics or background states of interest (e.g., TS, PRECT).

The solstice or equinox precession indices are defined as $e\sin(\widetilde{\omega})$ and $-e\cos(\widetilde{\omega})$, respectively, where the e is Earth's orbital eccentricity and $\widetilde{\omega}$ is the longitude of perihelion, measured as the angular distance from the moving vernal equinox to perihelion along Earth's orbit minus 180°.

Following previous study[117], we quantify the degree of asymmetry using a normalized asymmetry metric:

$$Asym = \frac{\alpha_{pos} - \alpha_{neg}}{\alpha_{pos} + \alpha_{neg}} \tag{2}$$

Having obtained regression parameters, the precession-modulated changes in a given variable can be reconstructed as:

$$\hat{F}|_p = \begin{cases} \alpha_{pos} \times p + \beta_{pos} \left(p > 0\right) \\ \alpha_{neg} \times p + \beta_{neg} \left(p < 0\right) \end{cases} \tag{3}$$

where all symbols follow the definitions in Eq. (1), and $\hat{F}|_p$ denotes the reconstructed value of F using either the solstice or equinox precession index p.

The Eq. (3) allows us to statistically estimate precession-induced ENSO changes at any desired chunk and compare relative changes across chunks. For example, the reconstructed difference in ENSO TS variance between the middle Holocene (mH) and preindustrial (PI) periods is given by:

$$\Delta var = \left(\hat{var}|_{p_{sols}}^{mH} + \hat{var}|_{p_{equi}}^{mH}\right) - \left(\hat{var}|_{psols}^{PI} + \hat{var}|_{p_{equi}}^{PI}\right) \tag{4}$$

where *var* denotes the millennial-resolution interannual TS variance over the tropical Pacific, and P_{sols} and P_{equi} are the solstice and equinox precession indices at the corresponding time slices (i.e., 6ka for mH and PI). A similar calculation can be applied to estimate ENSO variance differences between the LGM (21 ka) and PI periods.

For calculation of precession parameters, the orbital eccentricity values at LGM, mH, and PI are 0.018990, 0.018680, and 0.016724, respectively, with the corresponding longitudes of perihelion of 114.43°, 0.87°, and 102.04°. This regression-based framework provides a better isolation of the precipitation-driven ENSO response than direct comparisons of raw ENSO variability across individual 10-super-model-year chunks, which remain influenced by other external forcings and internal climate variability (Supplementary Fig. 9).

RO model

To investigate how solstice precession modulates ENSO variability intensity, we employ a theoretical linear RO framework under a classic configuration[71,118,119]:

$$\begin{cases} \frac{dT}{dt} = a_{11}T + a_{12}h + \sigma_T \xi_T \\ \frac{dh}{dt} = a_{21}T + a_{22}h + \sigma_h \xi_h \end{cases} \tag{5}$$

where T and h represent interannual TS anomalies over the Niño 3 region (90°–150°W, 5°S–5°N) and zonally averaged sea surface height anomalies across the equatorial Pacific (120°E–80°W, 5°S–5°N), respectively. The parameters a_{11} and a_{22} represent growth rates of TS and sea surface height anomalies, and together determine the instability of the coupled system. The coefficients a_{12} and a_{21} denote the coupling between TS and sea surface height, governing ENSO phase transitions and periodicity. The terms σ_T and σ_h denote the amplitudes of unresolved residuals that represent the strength of stochastic disturbances from the sea surface and ocean interior, while ξ_T and ξ_h refer to normalized Gaussian noise processes of short memory.

Millennial-resolution RO parameters are estimated using least-squares fitting within each data chunk (i.e., 10 super-model years), with time-tendency terms discretized via the central finite-difference scheme. After deriving the RO parameters, we perform three sets of stochastic RO simulations by perturbing the parameters within each chunk[120]. The first experiment retains all chunk-specific parameters and is used to evaluate how well the RO model captures temporal variations in ENSO activity. The other two sensitivity experiments isolate the influences of different physical processes by retaining only: (i) chunk-specific a_{11} and a_{22} parameters (BJ only), or (ii) chunk-specific ξ_T and ξ_h parameters (noise only), while setting all remaining parameters to their respective long-term means to eliminate their temporal variations. These experiments allow us to examine the relative roles of air–sea coupling and stochastic forcing in determining the asymmetric precessional modulation of ENSO variability strength. For each chunk, the RO model is integrated for 200 years with an ensemble of 50 members, and the ensemble-mean variance of simulated TS anomalies is analyzed.

Unlike ENSO amplitude, the thermocline-related processes are less effective at explaining zonal shifts in the center of ENSO variability in our simulation. Also, no well-established RO-based method exists to account for ENSO spatial diversity or its long-term modulation. Therefore, the RO framework is not applicable for investigating precession-induced changes in the zonal location of ENSO variability.

Data availability

The 3Ma simulation data are publicly available on the IBS Center for Climate Physics (ICCP) website: https://climatedata.ibs.re.kr/data/3ma-transient-climate-simulation. The diagnostic ENSO TS variance is available at ref. 121 https:/zenodo.org/records/18453260. The ERSSTv5 reanalysis is available on https://psl.noaa.gov/data/gridded/data.noaa.ersst.v5.html. The numerical solutions of orbital parameters by Laskar are derived from https://vo.imcce.fr/insola/earth/online/earth/earth.html.

Code availability

The Fortran code used to adjust the calendar effect of paleo-simulation is publicly available at https://github.com/pjbartlein/PaleoCalAdjust. The Python code for calculating the ENSO recharge oscillator parameters is available at https://github.com/senclimate/XRO. The code used in this study is available from C.L. (liuc@yonsei.ac.kr) upon request.

Received: 5 October 2025; Accepted: 10 February 2026;
Published online: 26 February 2026

References

1. McPhaden, M. J., Zebiak, S. E. & Glantz, M. H. ENSO as an integrating concept in Earth science. *Science* **314**, 1740–1745 (2006).
2. Callahan, C. W. & Mankin, J. S. Persistent effect of El Niño on global economic growth. *Science* **380**, 1064–1069 (2023).
3. Liu, Y., Cai, W., Lin, X., Li, Z. & Zhang, Y. Nonlinear El Niño impacts on the global economy under climate change. *Nat. Commun.* **14**, 5887 (2023).
4. Cai, W. et al. Increased ENSO sea surface temperature variability under four IPCC emission scenarios. *Nat. Clim. Chang*. **12**, 228–231 (2022).
5. Cai, W. et al. Changing El Niño–Southern Oscillation in a warming climate. *Nat. Rev. Earth Environ.* **2**, 628–644 (2021).
6. Cai, W. et al. Increased variability of eastern Pacific El Niño under greenhouse warming. *Nature* **564**, 201–206 (2018).
7. Shin, N.-Y. et al. More frequent central Pacific El Niño and stronger eastern Pacific El Niño in a warmer climate. *NPJ Clim. Atmos. Sci.* **5**, 101 (2022).
8. Yeh, S.-W. et al. El Niño in a changing climate. *Nature* **461**, 511–514 (2009).
9. Wang, B. et al. Historical change of El Niño properties sheds light on future changes of extreme El Niño. *Proc. Natl. Acad. Sci.* **116**, 22512–22517 (2019).
10. Liu, C. et al. Hysteresis of the El Niño–Southern oscillation to CO_2 forcing. *Sci. Adv*. **9**, eadh8442 (2023).
11. Liu, Z. et al. Evolution and forcing mechanisms of El Niño over the past 21,000 years. *Nature* **515**, 550–553 (2014).
12. Lu, Z., Liu, Z., Chen, G. & Guan, J. Prominent precession band variance in ENSO intensity over the last 300,000 years. *Geophys. Res. Lett.* **46**, 9786–9795 (2019).
13. Erb, M. P., Broccoli, A. J. & Clement, A. C. The contribution of radiative feedbacks to orbitally driven climate change. *J. Clim.* **26**, 5897–5914 (2013).
14. Mandal, G. et al. Northern Hemisphere sea ice variability in a transient CGCM simulation of the past 2.6 Ma. *Nat. Commun.* **16**, 39 (2025).
15. Gerber, L. et al. Low variability of the Atlantic Meridional Overturning Circulation throughout the Holocene. *Nat. Commun.* **16**, 6748 (2025).
16. Liu, Z. Evolution of Atlantic Meridional Overturning Circulation since the last glaciation: model simulations and relevance to present and future. *Philos. Trans. Royal Soc. A: Math. Phys. Eng. Sci.* **381**, 20220190 (2023).
17. An, Z. et al. Mid-Pleistocene climate transition triggered by Antarctic Ice Sheet growth. *Science* **385**, 560–565 (2024).
18. Thirumalai, K. et al. Future increase in extreme El Niño supported by past glacial changes. *Nature* **634**, 374–380 (2024).
19. Tierney, J. E. et al. Past climates inform our future. *Science*. **370**, eaay3701 (2020).
20. Saint-Lu, M., Braconnot, P., Leloup, J., Lengaigne, M. & Marti, O. Changes in the ENSO/SPCZ relationship from past to future climates. *Earth Planet. Sci. Lett.* **412**, 18–24 (2015).
21. Pontes, G. M., da Silva Dias, P. L. & Menviel, L. Rapid communication: Nonlinear sensitivity of the El Niño–Southern Oscillation across climate states. *Clim. Past* **21**, 1079–1091 (2025).
22. Lu, Z. & Liu, Z. Examining El Niño in the Holocene: implications and challenges. *Natl. Sci. Rev.* **5**, 807–809 (2018).
23. Sandweiss, D. H., Richardson, J. B., Reitz, E. J., Rollins, H. B. & Maasch, K. A. Geoarchaeological evidence from Peru for a 5000 Years B.P. Onset of El Niño. *Science* **273**, 1531–1533 (1996).
24. Sandweiss, D. H. et al. Variation in Holocene El Niño frequencies: Climate records and cultural consequences in ancient Peru. *Geology* **29**, 603 (2001).
25. Zhou, P. et al. Mid to late Holocene ENSO variability reconstructed by high-resolution Tridacna Sr/Ca records from the northern part of the South China Sea. *Palaeogeogr. Palaeoclimatol. Palaeoecol.* **601**, 111117 (2022).
26. McGregor, H. V. & Gagan, M. K. Western Pacific coral $\delta^{18}O$ records of anomalous Holocene variability in the El Niño–Southern Oscillation. *Geophys. Res. Lett*. **31**, L11204 (2004).
27. Otto-Bliesner, B. L. El Niño/La Niña and Sahel precipitation during the Middle Holocene. *Geophys. Res. Lett.* **26**, 87–90 (1999).
28. Liu, Z., Kutzbach, J. & Wu, L. Modeling climate shift of El Nino variability in the Holocene. *Geophys. Res. Lett.* **27**, 2265–2268 (2000).
29. Otto-Bliesner, B. L., Brady, E. C., Shin, S., Liu, Z. & Shields, C. Modeling El Niño and its tropical teleconnections during the last glacial-interglacial cycle. *Geophys. Res. Lett*. **30**, 2198 (2003).

30. Liu, Z., Brady, E. & Lynch-Stieglitz, J. Global ocean response to orbital forcing in the Holocene. *Paleoceanography* **18**,1041 (2003).
31. Brown, J., Collins, M., Tudhope, A. W. & Toniazzo, T. Modelling mid-Holocene tropical climate and ENSO variability: towards constraining predictions of future change with palaeo-data. *Clim. Dyn.* **30**, 19–36 (2007).
32. Clement, A. C., Seager, R. & Cane, M. A. Suppression of El Niño during the Mid-Holocene by changes in the Earth's orbit. *Paleoceanography* **15**, 731–737 (2000).
33. Braconnot, P., Luan, Y., Brewer, S. & Zheng, W. Impact of Earth's orbit and freshwater fluxes on Holocene climate mean seasonal cycle and ENSO characteristics. *Clim. Dyn.* **38**, 1081–1092 (2012).
34. Clement, A. C., Seager, R. & Cane, M. A. Orbital controls on the El Niño/Southern Oscillation and the tropical climate. *Paleoceanography* **14**, 441–456 (1999).
35. Liu, Z. A simple model study of ENSO suppression by external periodic forcing*. *J. Clim.* **15**, 1088–1098 (2002).
36. Timmermann, A., Lorenz, S. J., An, S.-I., Clement, A. & Xie, S.-P. The effect of orbital forcing on the mean climate and variability of the Tropical Pacific. *J. Clim.* **20**, 4147–4159 (2007).
37. Chiang, J. C. H., Fang, Y. & Chang, P. Pacific Climate Change and ENSO Activity in the Mid-Holocene. *J. Clim.* **22**, 923–939 (2009).
38. Pausata, F. S. R. et al. Greening of the Sahara suppressed ENSO activity during the mid-Holocene. *Nat. Commun.* **8**, 16020 (2017).
39. Moy, C. M., Seltzer, G. O., Rodbell, D. T. & Anderson, D. M. Variability of El Niño/Southern Oscillation activity at millennial timescales during the Holocene epoch. *Nature* **420**, 162–165 (2002).
40. Koutavas, A. & Joanides, S. El Niño–Southern Oscillation extrema in the Holocene and Last Glacial Maximum. *Paleoceanography* **27**, PA4208 (2012).
41. Conroy, J. L., Overpeck, J. T., Cole, J. E., Shanahan, T. M. & Steinitz-Kannan, M. Holocene changes in eastern tropical Pacific climate inferred from a Galápagos lake sediment record. *Quat. Sci. Rev.* **27**, 1166–1180 (2008).
42. Emile-Geay, J. et al. Links between tropical Pacific seasonal, interannual and orbital variability during the Holocene. *Nat. Geosci.* **9**, 168–173 (2016).
43. Chen, S. et al. A high-resolution speleothem record of western equatorial Pacific rainfall: Implications for Holocene ENSO evolution. *Earth Planet. Sci. Lett.* **442**, 61–71 (2016).
44. Rein, B. et al. El Niño variability off Peru during the last 20,000 years. *Paleoceanography* **20**, PA4003 (2005).
45. Karamperidou, C., Jin, F.-F. & Conroy, J. L. The importance of ENSO nonlinearities in tropical Pacific response to external forcing. *Clim. Dyn.* **49**, 2695–2704 (2016).
46. Karamperidou, C. & DiNezio, P. N. Holocene hydroclimatic variability in the tropical Pacific explained by changing ENSO diversity. *Nat. Commun.* **13**, 7244 (2022).
47. Lu, Z. & Liu, Z. Orbital modulation of ENSO seasonal phase locking. *Clim. Dyn.* **52**, 4329–4350 (2019).
48. Lu, Z., Liu, Z., Zhu, J. & Cobb, K. M. A review of Paleo El Niño-Southern Oscillation. *Atmosphere* **9**, 130 (2018).
49. Zheng, W. & Yu, Y. Paleoclimate simulations of the mid-Holocene and last glacial maximum by FGOALS. *Adv. Atmos. Sci.* **30**, 684–698 (2013).
50. Kageyama, M. et al. The PMIP4 contribution to CMIP6 – Part 4: Scientific objectives and experimental design of the PMIP4-CMIP6 Last Glacial Maximum experiments and PMIP4 sensitivity experiments. *Geosci. Model Dev.* **10**, 4035–4055 (2017).
51. Haywood, A. M. et al. The Pliocene Model Intercomparison Project (PlioMIP) Phase 2: scientific objectives and experimental design. *Climate of the Past* **12**, 663–675 (2016).
52. Oldeman, A. M. et al. Reduced El Niño variability in the mid-Pliocene according to the PlioMIP2 ensemble. *Clim. Past* **17**, 2427–2450 (2021).
53. Ford, H. L., Ravelo, A. C. & Polissar, P. J. Reduced El Niño–Southern oscillation during the last glacial maximum. *Science* **347**, 255–258 (2015).
54. Zheng, W., Braconnot, P., Guilyardi, E., Merkel, U. & Yu, Y. ENSO at 6ka and 21ka from ocean–atmosphere coupled model simulations. *Clim. Dyn.* **30**, 745–762 (2008).
55. Brady, E. C., Otto-Bliesner, B. L., Kay, J. E. & Rosenbloom, N. Sensitivity to glacial forcing in the CCSM4. *J. Clim.* **26**, 1901–1925 (2013).
56. Pontes, G. M. et al. Mid-Pliocene El Niño/Southern Oscillation suppressed by Pacific intertropical convergence zone shift. *Nat. Geosci.* **15**, 726–734 (2022).
57. White, S. M., Ravelo, A. C. & Polissar, P. J. Dampened El Niño in the Early and Mid-Holocene due to insolation-forced warming/deepening of the Thermocline. *Geophys. Res. Lett.* **45**, 316–326 (2018).
58. Lu, Z. et al. Increased frequency of multi-year El Niño–Southern Oscillation events across the Holocene. *Nat. Geosci.* **18**, 337–343 (2025).
59. Watanabe, T. et al. Permanent El Niño during the Pliocene warm period not supported by coral evidence. *Nature* **471**, 209–211 (2011).
60. Emile-Geay, J., Cobb, K. M., Cole, J. E., Elliot, M. & Zhu, F. Past ENSO Variability. In *El Niño Southern Oscillation in a Changing Climate* 87–118. https://doi.org/10.1002/9781119548164.ch5. (2020).
61. Yun, K.-S. et al. A transient coupled general circulation model (CGCM) simulation of the past 3 million years. *Clim. Past* **19**, 1951–1974 (2023).
62. Callahan, C. W. et al. Robust decrease in El Niño/Southern Oscillation amplitude under long-term warming. *Nat. Clim. Chang.* **11**, 752–757 (2021).
63. Kim, S.-K. et al. Decreased Indian Ocean Dipole variability under prolonged greenhouse warming. *Nat. Commun.* **15**, 2811 (2024).
64. Clement, A. C., Hall, A. & Broccoli, A. J. The importance of precessional signals in the tropical climate. *Clim. Dyn.* **22**, 327–341 (2004).
65. Clement, A. C., Cane, M. A. & Seager, R. An orbitally driven tropical source for abrupt climate change*. *J. Clim.* **14**, 2369–2375 (2001).
66. Erb, M. P. et al. Response of the Equatorial Pacific seasonal cycle to orbital forcing. *J. Clim.* **28**, 9258–9276 (2015).
67. Wang, Y. et al. Precessional Forced Zonal Triple-Pole Anomalies in the Tropical Pacific Annual Cycle. *J. Clim.* **32**, 7369–7402 (2019).
68. Jin, F. et al. Simple ENSO Models. In 119–151. https://doi.org/10.1002/9781119548164.ch6. (2020).
69. Timmermann, A. et al. El Niño–Southern Oscillation complexity. *Nature* **559**, 535–545 (2018).
70. Liu, C. et al. ENSO skewness hysteresis and associated changes in strong El Niño under a CO_2 removal scenario. *NPJ Clim. Atmos. Sci.* **6**, 117 (2023).
71. Jin, F.-F. An Equatorial Ocean Recharge Paradigm for ENSO. Part I: conceptual model. *J. Atmos. Sci.* **54**, 811–829 (1997).
72. Jin, F.-F., Kim, S. T. & Bejarano, L. A coupled-stability index for ENSO. *Geophys. Res. Lett.* **33**, L23708 (2006).
73. Bunge, L. & Clarke, A. J. On the warm water volume and its changing relationship with ENSO. *J. Phys. Oceanogr.* **44**, 1372–1385 (2014).
74. Abhik, S. et al. Stronger and prolonged El Niño-Southern Oscillation in the Early Eocene warmth. *Nat. Commun.* **16**, 4053 (2025).
75. Cai, W. et al. Increasing frequency of extreme El Niño events due to greenhouse warming. *Nat. Clim. Chang.* **4**, 111–116 (2014).
76. Santoso, A., Mcphaden, M. J. & Cai, W. The defining characteristics of ENSO extremes and the strong 2015/2016 El Niño. *Rev. Geophys.* **55**, 1079–1129 (2017).
77. Kim, W., Cai, W. & Kug, J.-S. Migration of atmospheric convection coupled with ocean currents pushes El Niño to extremes. *Geophys. Res. Lett.* **42**, 3583–3590 (2015).

78. Pathirana, G. et al. Increase in convective extreme El Niño events in a CO_2 removal scenario. *Sci. Adv*. **9**, eadh2412 (2023).
79. Kug, J.-S., Jin, F.-F. & An, S.-I. Two Types of El Niño Events: Cold Tongue El Niño and Warm Pool El Niño. *J. Clim.* **22**, 1499–1515 (2009).
80. Ren, H.-L. & Jin, F.-F. Recharge oscillator mechanisms in two types of ENSO. *J. Clim.* **26**, 6506–6523 (2013).
81. Vecchi, G. A. & Soden, B. J. Effect of remote sea surface temperature change on tropical cyclone potential intensity. *Nature* **450**, 1066–1070 (2007).
82. Xie, S.-P. et al. Global warming pattern formation: sea surface temperature and rainfall. *J. Clim.* **23**, 966–986 (2010).
83. Lin, Y., Zhao, M. & Zhang, M. Tropical cyclone rainfall area controlled by relative sea surface temperature. *Nat. Commun.* **6**, 6591 (2015).
84. Izumo, T., Vialard, J., Lengaigne, M. & Suresh, I. Relevance of relative sea surface temperature for tropical rainfall interannual variability. *Geophys. Res. Lett*. **47**, e2019GL086182 (2020).
85. L'Heureux, M. L. et al. A relative sea surface Temperature Index for Classifying ENSO events in a changing climate. *J. Clim.* **37**, 1197–1211 (2024).
86. Huang, P. & Xie, S.-P. Mechanisms of change in ENSO-induced tropical Pacific rainfall variability in a warming climate. *Nat. Geosci.* **8**, 922–926 (2015).
87. Liu, C., An, S.-I., Yan, Z., Kim, S.-K. & Paik, S. Strong El Niño and La Niña precipitation—sea surface temperature sensitivity under a carbon removal scenario. *Commun. Earth Environ.* **5**, 774 (2024).
88. Zheng, X.-T., Xie, S.-P., Lv, L.-H. & Zhou, Z.-Q. Intermodel Uncertainty in ENSO amplitude change tied to Pacific Ocean warming pattern. *J. Clim.* **29**, 7265–7279 (2016).
89. Huang, P. Time-varying response of ENSO-induced tropical Pacific rainfall to global warming in CMIP5 Models. Part II: Intermodel uncertainty. *J. Clim.* **30**, 595–608 (2017).
90. An, S., Tziperman, E., Okumura, Y. M. & Li, T. ENSO irregularity and asymmetry. *El Niño Southern Oscillation in a Changing Climate* 153–172 (2020).
91. Merlis, T. M., Schneider, T., Bordoni, S. & Eisenman, I. The tropical precipitation response to orbital precession. *J. Clim.* **26**, 2010–2021 (2013).
92. Tigchelaar, M. & Timmermann, A. Mechanisms rectifying the annual mean response of tropical Atlantic rainfall to precessional forcing. *Clim. Dyn.* **47**, 271–293 (2016).
93. Xie, S.-P. & Philander, S. G. H. A coupled ocean-atmosphere model of relevance to the ITCZ in the eastern Pacific. *Tellus A: Dyn. Meteorol. Oceanogr.* **46**, 340 (1994).
94. Chiang, J. C. H., Fang, Y. & Chang, P. Interhemispheric thermal gradient and tropical Pacific climate. *Geophys. Res. Lett*. **35**, L14704 (2008).
95. Berger, A. Long-term variations of daily insolation and quaternary climatic changes. *J. Atmos. Sci.* **35**, 2362–2367 (1978).
96. Laskar, J. et al. A long-term numerical solution for the insolation quantities of the Earth. *Astron. Astrophys.* **428**, 261–285 (2004).
97. Chiang, J. C. H. et al. Two annual cycles of the Pacific cold tongue under orbital precession. *Nature* **611**, 295–300 (2022).
98. Chen, L., Wang, L., Li, T. & Liu, J. Drivers of reduced ENSO variability in mid-Holocene in a coupled model. *Clim. Dyn.* **52**, 5999–6014 (2019).
99. Shields, C. A. et al. The low-resolution CCSM4. *J. Clim.* **25**, 3993–4014 (2012).
100. Su, B., Sun, Y. & Zhou, M. Orbital-accelerated transient simulations of glacial-interglacial climate cycles for the last 800,000 years. *Sci. Data* **12**, 961 (2025).
101. Yang, H. et al. Precession-driven low-latitude hydrological cycle paced by shifting perihelion. *Clim. Past* **21**, 1263–1279 (2025).
102. Persch, C. F. & Sanchez, S. C. A critical role for North Pacific Meridional Mode in the ENSO response to orbital precession. *J. Clim.* **38**, 6545–6558 (2025).
103. Hurrell, J. W. et al. The Community Earth System Model: A Framework for Collaborative Research. *Bull. Am. Meteorol. Soc.* **94**, 1339–1360 (2013).
104. Jian, Z. et al. Warm pool ocean heat content regulates ocean–continent moisture transport. *Nature* **612**, 92–99 (2022).
105. Bereiter, B. et al. Revision of the EPICA Dome C CO_2 record from 800 to 600 kyr before present. *Geophys. Res. Lett.* **42**, 542–549 (2015).
106. Willeit, M., Ganopolski, A., Calov, R. & Brovkin, V. Mid-Pleistocene transition in glacial cycles explained by declining CO_2 and regolith removal. *Sci. Adv*. **5**, eaav7337 (2019).
107. Lisiecki, L. E. & Raymo, M. E. A Pliocene-Pleistocene stack of 57 globally distributed benthic δ^{18} O records. *Paleoceanography* **20**, PA1003 (2005).
108. Timmermann, A. et al. The influence of a weakening of the Atlantic meridional overturning circulation on ENSO. *J. Clim.* **20**, 4899–4919 (2007).
109. Argus, D. F., Peltier, W. R., Drummond, R. & Moore, A. W. The Antarctica component of postglacial rebound model ICE-6G_C (VM5a) based on GPS positioning, exposure age dating of ice thicknesses, and relative sea level histories. *Geophys. J. Int.* **198**, 537–563 (2014).
110. Di Nezio, P. N. et al. The climate response of the Indo-Pacific warm pool to glacial sea level. *Paleoceanography* **31**, 866–894 (2016).
111. Park, H.-J., An, S.-I., Park, J.-H. & Liu, C. Unraveling the interactions between tropical Indo-Pacific climate modes using a simple model framework. *NPJ Clim. Atmos. Sci.* **8**, 336 (2025).
112. Huang, B. et al. Extended reconstructed sea surface temperature, Version 5 (ERSSTv5): Upgrades, validations, and intercomparisons. *J. Clim.* **30**, 8179–8205 (2017).
113. Joussaume, S. & Braconnot, P. Sensitivity of paleoclimate simulation results to season definitions. *J. Geophys. Res.: Atmos.* **102**, 1943–1956 (1997).
114. Bartlein, P. J. & Shafer, S. L. Paleo calendar-effect adjustments in time-slice and transient climate-model simulations (PaleoCalAdjust v1.0): impact and strategies for data analysis. *Geosci. Model Dev.* **12**, 3889–3913 (2019).
115. Duchon, C. E. Lanczos filtering in one and two dimensions. *J. Appl. Meteorol.* **18**, 1016–1022 (1979).
116. Frankignoul, C. & Kwon, Y. On the statistical estimation of asymmetrical relationship between two climate variables. *Geophys. Res. Lett*. **49**, e2022GL100777 (2022).
117. An, S.-I. & Kim, J.-W. Role of nonlinear ocean dynamic response to wind on the asymmetrical transition of El Niño and La Niña. *Geophys. Res. Lett.* **44**, 393–400 (2017).
118. Zhao, S. et al. Explainable El Niño predictability from climate mode interactions. *Nature* **630**, 891–898 (2024).
119. Vialard, J. et al. The El Niño Southern Oscillation (ENSO) recharge oscillator conceptual model: achievements and future prospects. *Rev. Geophys.* **63**, (2025).
120. Wengel, C., Dommenget, D., Latif, M., Bayr, T. & Vijayeta, A. What controls ENSO-amplitude diversity in climate models? *Geophys. Res. Lett.* **45**, 1989–1996 (2018).
121. Liu, C. et al. Data associated with: Precessional modulation of ENSO strength and spatial structure in a transient CGCM simulation of the past 3 million years. Zenodo https://doi.org/10.5281/zenodo.18453260 (2026).

Acknowledgements

We thank Dr. Axel Timmermann for his constructive suggestions provided at the early stage of this work. This work was funded by the Korea Meteorological Administration Research and Development Program (RS-2025-02313090) and by the National Research Foundation of Korea (NRF)

grant funded by the Korean government (NRF-2022R1A3B1077622). S.I.A. was supported by the Yonsei Signature Research Cluster Program (2021-22-0003) and the Yonsei Fellowship, funded by Lee Youn Jae.

Author contributions

C.L., S.I.A., and J.S.K. conceived the idea. C.L. conducted the analysis, wrote the initial draft of the manuscript, and produced all figures. S.I.A. guided the research and oversaw the project. K.S.Y. provided the 3 Ma simulation data. K.S.Y. and G.M. offered suggestions on the data processing and the research background of paleoclimate. S.I.A., S.K.K., J.S.K., and F.F.J. offered suggestions on the RO model. All authors contributed to the interpretation of the results and improvement of the manuscript.

Competing interests

The authors declare no competing interests.

Additional information

Supplementary information The online version contains supplementary material available at https://doi.org/10.1038/s41612-026-01355-2.

Correspondence and requests for materials should be addressed to Soon-Il An or Jong-Seong Kug.

Reprints and permissions information is available at http://www.nature.com/reprints

Publisher's note Springer Nature remains neutral with regard to jurisdictional claims in published maps and institutional affiliations.

Open Access This article is licensed under a Creative Commons Attribution-NonCommercial-NoDerivatives 4.0 International License, which permits any non-commercial use, sharing, distribution and reproduction in any medium or format, as long as you give appropriate credit to the original author(s) and the source, provide a link to the Creative Commons licence, and indicate if you modified the licensed material. You do not have permission under this licence to share adapted material derived from this article or parts of it. The images or other third party material in this article are included in the article's Creative Commons licence, unless indicated otherwise in a credit line to the material. If material is not included in the article's Creative Commons licence and your intended use is not permitted by statutory regulation or exceeds the permitted use, you will need to obtain permission directly from the copyright holder. To view a copy of this licence, visit http://creativecommons.org/licenses/by-nc-nd/4.0/.

© The Author(s) 2026